

**Variational regional inverse modeling of reactive species emissions**  
**with PYVAR-CHIMERE-v2019**

Audrey Fortems-Cheiney<sup>1</sup>, Isabelle Pison<sup>1</sup>, Grégoire Broquet<sup>1</sup>, Gaëlle Dufour<sup>2</sup>, Antoine Berchet<sup>1</sup>,  
Elise Potier<sup>1</sup>, Adriana Coman<sup>2</sup>, Guillaume Siour<sup>2</sup>, and Lorenzo Costantino<sup>2</sup>

<sup>1</sup>Laboratoire des Sciences du Climat et de l'Environnement, LSCE-IPSL (CEA-CNRS-UVSQ),  
Université Paris-Saclay, 91191 Gif-sur-Yvette, France.

<sup>2</sup>Laboratoire Interuniversitaire des Systèmes Atmosphériques, UMR CNRS 7583, Université Paris  
Est Créteil et Université Paris Diderot, Institut Pierre Simon Laplace, Créteil, France.

**Abstract**

Up-to-date and accurate emission inventories for air pollutants are essential for understanding their role in the formation of tropospheric ozone and particulate matter at various temporal scales, for anticipating pollution peaks and for identifying the key drivers that could help mitigate their concentrations. This paper describes the Bayesian variational inverse system PYVAR-CHIMERE, which is now adapted to the inversion of reactive species. Complementarily with bottom-up inventories, this system aims at updating and improving the knowledge on the high spatio-temporal variability of emissions of air pollutants and their precursors. The system is designed to use any type of observations, such as satellite observations or surface station measurements. The potential of PYVAR-CHIMERE is illustrated with inversions of both CO and NO<sub>x</sub> emissions in Europe, using the MOPITT and OMI satellite observations, respectively. In these cases, local increments on CO emissions can reach more than +50%, with increases located mainly over Central and Eastern Europe, except in the south of Poland, and decreases located over Spain and Portugal. The illustrative cases for NO<sub>x</sub> emissions also lead to large local increments (> 50%), for example over industrial areas (e.g., over the Po Valley) and over the Netherlands. The good behavior of the inversion is shown through statistics on the concentrations: the mean bias, RMSE, standard deviation and correlation between the simulated and observed concentrations. For CO, the mean bias is reduced by about 27% when using the posterior emissions, the RMSE and the standard deviation are reduced by about 50% and the correlation is strongly improved (0.74 when using the posterior emissions against 0.02); for NO<sub>x</sub>, the mean bias is reduced by about 24%, the RMSE and the standard deviation are reduced by about 7% but the correlation is not improved. We reported strong non-linear relationships between NO<sub>x</sub> emissions and satellite NO<sub>2</sub> columns, now requiring a fully comprehensive scientific study.

## 1. Introduction

The degradation of air quality is a worldwide environmental problem: 91% of the world's population have breathed polluted air in 2016 according to the World Health Organization (WHO), resulting in 4.2 millions of premature deaths every year [WHO, 2016]. The recent study of Lelieveld et al. [2019] even suggests that the health impacts attributable to outdoor air pollution are substantially higher than previously assumed (with 790,000 premature deaths in the 28 countries of the European Union against the previously estimated 500,000 [EEA, 2018]). The main regulated primary (i.e. directly emitted in the atmosphere) anthropogenic air pollutants are carbon monoxide (CO), nitrogen oxides ( $\text{NO}_x = \text{NO} + \text{NO}_2$ ), sulfur dioxide ( $\text{SO}_2$ ), ammonia ( $\text{NH}_3$ ), volatile organic compounds (VOCs), and primary particles. These primary air pollutants are precursors of secondary (i.e. produced in the atmosphere through chemical reactions) pollutants such as ozone ( $\text{O}_3$ ) and Particulate Matter (PM), which are also threatening to both human health and ecosystems. Monitoring concentrations and quantifying emissions are still challenging and limit our capability to forecast air quality to warn population and to assess i) the exposure of population to air pollution and ii) the efficiency of mitigation policies.

Bottom-up (BU) inventories are built in the framework of air quality policies such as The Convention on Long-Range Transboundary Air Pollution (LRTAP, <http://www.unece.org>) for air pollutants. Based on national annual inventories, research institutes compile gridded global or regional, monthly inventories (mainly for the US, Europe and China) with a high spatial resolution (currently regional or city scale inventories are typically finer than  $0.1^\circ \times 0.1^\circ$ ). These inventories are constructed by combining available (economic) statistics data from different detailed activity sectors with the most appropriate emission factors (defined as the average emission rate of a given species for a given source or process, relative to the unit of activity in a given administrative area). It is important to note that the activity data (often statistical data) has an inherent uncertainty and that its reliability may vary between countries or regions. In addition, the emission factors bear large uncertainties in their quantification [Kuenen et al., 2014; EMEP/EEA, 2016; Kurokawa et al., 2013]. Moreover, these inventories are often provided at the annual or monthly scale with typical temporal profiles to build the weekly, daily and hourly variability of the emissions. The combination of uncertain activity data, emission factors and emission timing can be a large source of uncertainties, if not errors, for forecasting or analyzing air quality [Menut et al., 2012]. Finally, since updating the inventories and gathering the required data for a given year is costly in time, manpower and money, only a few institutes have offered estimates of the gaseous pollutants for each year since 2011 (i.e, European Monitoring and Evaluation Programme EMEP updated until the year 2017, MEIC updated until the year 2017 to our knowledge). Nevertheless, using knowledge

72 from inventories and air quality modeling, emissions have been mitigated. For example, from 2010  
73 to nowadays, emissions in various countries have been modified and/or regional trends have been  
74 reversed downwards (e.g., the decrease of NO<sub>x</sub> emissions over China since 2011 [de Foy et al.,  
75 2016]), leading to significant changes in the atmospheric composition. Consequently, the  
76 knowledge of precise and updated budgets, together with seasonal, monthly, weekly and daily  
77 variations of gaseous pollutants driven, amongst other processes, by the emissions are essential for  
78 understanding their role in the formation of tropospheric ozone and PMs at various temporal scales,  
79 for anticipating pollution peaks and for identifying the key drivers that could help mitigate these  
80 concentrations.

81

82 In this context, complementary methods have been developed for estimating emissions using  
83 atmospheric observations. They operate in synergy between a chemistry-transport model (CTM)  
84 which links the emissions to the atmospheric concentrations, atmospheric observations of the  
85 species of interest, and statistical inversion techniques. A number of studies using inverse modeling  
86 were first carried out for long-lived species such as greenhouses gases (GHGs) (e.g., carbon dioxide  
87 CO<sub>2</sub> or methane CH<sub>4</sub>) at the global or continental scales [Hein et al., 1997; Bousquet et al. 1999],  
88 using surface measurements. Later, following the development of monitoring station networks, the  
89 progress of computing power, and the use of inversion techniques more appropriate to non-linear  
90 problems, these methods were applied to shorter-lived molecules such as CO. For these various  
91 applications (e.g., for CO<sub>2</sub>, CH<sub>4</sub>, CO), the quantification of sources was solved at the resolution of  
92 large regions [Pétron et al., 2002]. Finally, the growing availability and reliability of observations  
93 since the early 2000s (in-situ surface data, remote sensing data such as satellite data), the  
94 improvement of the global CTMs, of the computational capacities and of the inversion techniques  
95 have increased the achievable resolution of global inversions, up to the global transport model grid  
96 cells, i.e. typically with a spatial resolution of several hundreds of square kilometers [Stavrakou and  
97 Muller, 2006; Pison et al., 2009; Fortems-Cheiney et al., 2011; Hooghiemstra et al., 2012; Yin et  
98 al., 2015; Miyazaki et al., 2017, Zheng et al., 2019].

99

100 Today, the scientific and societal issues require an up-to-date quantification of pollutant emissions  
101 at a higher spatial resolution than the global one and imply to widely use regional inverse systems.  
102 However, although they are suited to reactive species such as CO and NO<sub>x</sub>, and their very large  
103 spatial and temporal variability, they have hardly been used to quantify pollutant emissions. Some  
104 studies inferred NO<sub>x</sub> [Pison et al., 2007; Tang et al., 2013] and VOC emissions [Koohkan et al.,  
105 2013] from surface measurements. Konovalov et al. [2006, 2008, 2010], Mijling et al. [2012, 2013],  
106 van der A et al. [2008], Lin et al. [2012] and Ding et al. [2017] have also shown that satellite

107 observations are a suitable source of information to constrain  $\text{NO}_x$  emissions. These regional  
108 inversions using satellite observations were often based on Kalman Filter (KF) schemes [Mijling et  
109 al., 2012, 2013; van der A et al., 2008; Lin et al., 2012; Ding et al., 2017].

110

111 Variational inversion systems allow solving for high dimensional problems, typically solving for  
112 the fluxes at high spatial and temporal resolution, which can be critical to fully exploit satellite  
113 images. Here, we present the Bayesian variational atmospheric inversion system PYVAR-  
114 CHIMERE for the monitoring of anthropogenic emissions of reactive species at the regional scale.  
115 It is based on the Bayesian variational assimilation code PYVAR [Chevallier et al. 2005] and on the  
116 regional state-of-the-art CTM CHIMERE [Menut et al., 2013; Mailler et al., 2017]. CHIMERE is  
117 dedicated to the study of regional atmospheric pollution events [e.g., Ciarelli et al., 2019; Menut et  
118 al., 2020], included in the operational ensemble of the Copernicus Atmosphere Monitoring Service  
119 (CAMS) regional services. The main strengths of PYVAR-CHIMERE come from the strengths of  
120 CHIMERE and from its high modularity for the definition of the control vector. CHIMERE is  
121 indeed an extremely flexible code, in particular for the definition of the chemical scheme.

122 The PYVAR-CHIMERE system takes advantage of the previous developments for the  
123 quantification of fluxes of long-lived GHG species such as  $\text{CO}_2$  [Broquet et al., 2011] and  $\text{CH}_4$   
124 [Pison et al., 2018] at the regional to the local scales, but now solves for reactive species such as CO  
125 and  $\text{NO}_x$ . It has also a better level of robustness, clarity, portability, and modularity than these  
126 previous systems. Variational techniques require the adjoint of the model to compute the sensitivity  
127 of simulated atmospheric concentrations to corrections of the fluxes. CHIMERE is one of the few  
128 CTMs for which the adjoint has been coded. For global models, they include: GEOS-CHEM  
129 [Henze et al., 2007], IMAGES [Stavrakou and Muller, 2006], TM5 [Krol et al., 2008], GELKA  
130 [Belikov et al., 2016] and LMDz [Chevallier et al., 2005; Pison et al., 2009] ; for limited-area  
131 models they include: CMAQ [Hakami et al., 2007], EURAD-IM [Elbern et al., 2007],  
132 RAMS/CTM-4DVAR [Yumimoto et Uno, 2006], WRF-CO2 4D-Var [Zheng et al., 2018]).

133

134 The principle of variational atmospheric inversion and the configuration of PYVAR-CHIMERE are  
135 described in Section 2 and in Section 3, respectively. Details about the forward, tangent-linear and  
136 adjoint codes of CHIMERE are also given. Then, the potential of PYVAR-CHIMERE is illustrated  
137 in Section 4 with the optimization of European CO and  $\text{NO}_x$  emissions, constrained by observations  
138 from the Measurement of Pollution in the Troposphere (MOPITT) and from the Ozone Monitoring  
139 Instrument (OMI) satellite instruments, respectively.

140

141

## 142 2. Principle of Bayesian variational atmospheric inversion

143 In what follows, we use the notations and equations used in the inverse modeling community  
144 [Rayner et al., 2019]. The Bayesian variational atmospheric inversion method adjusts a set of  
145 control parameters, including parameters related to the emissions whose estimate is the primary  
146 target of the inversion.

147 The prior information about the parameters  $\mathbf{x}$  to be optimized during the inversion process is given  
148 by the vector  $\mathbf{x}^b$ . The parameters to be optimized can be surface fluxes but may also include initial  
149 or boundary conditions for example, as explained in Section 3.4. The adjustments are applied to  
150 prior values, usually taken, for the emissions, from pre-existing BU inventories. The principle is to  
151 minimize, on the one hand, the departures from the prior estimates of the control parameters, which  
152 are weighted by the uncertainties in these estimates (called hereafter “prior uncertainties”), and, on  
153 the other hand, the differences between simulated and observed concentrations, which are weighted  
154 by all other sources of uncertainties explaining these differences (called hereafter all together  
155 “observation errors”). In statistical terms, the inversion searches for the most probable estimate of  
156 the control parameters given their prior estimates, observations, CTM and their associated  
157 uncertainties. The solution, which will be called posterior estimate, is found by the iterative  
158 minimization of a cost function  $J$  [Talagrand et al., 1997], defined as:

$$159 J(\mathbf{x}) = (\mathbf{x} - \mathbf{x}^b)^T \mathbf{B}^{-1}(\mathbf{x} - \mathbf{x}^b) + (H(\mathbf{x}) - \mathbf{y})^T \mathbf{R}^{-1}(H(\mathbf{x}) - \mathbf{y}) \quad (\text{Eq. 1})$$

160  
161  $H$  is the non-linear observation operator that projects the control vector  $\mathbf{x}$  onto the observation  
162 space. In most of the variational atmospheric inversion cases (such as those described in Section 4),  
163 the observation operator includes the operations performed by the CTM in linking the emissions to  
164 the concentrations and any other transformation to compute the simulated equivalent of the  
165 observations such as an interpolation or an extraction and averaging of the simulated concentration  
166 fields (see Section 3.5). The observations in  $\mathbf{y}$  could be surface measurements and/or remote sensing  
167 data such as satellite data. The prior uncertainties and the observation errors are assumed to be  
168 unbiased and to have a Gaussian distribution. Consequently, the prior uncertainties are  
169 characterized by their covariance matrix  $\mathbf{B}$  and the observation errors are characterized by their  
170 covariance matrix  $\mathbf{R}$ . By definition, the observation errors combine errors in both the data and the  
171 observation operator, in particular measurement errors and errors in the conversion of satellite  
172 measurement into concentration data, errors from the CTM, representativity errors due to the  
173 comparison between point measurements and gridded models or due to the representation of the  
174 fluxes as gridded maps at a given spatial resolution, and aggregation errors associated with the  
175 optimization of emissions at a given spatial and/or temporal resolution (as specified in the control  
176 vector) that is different from (usually coarser than) that of the CTM [Wang et al., 2017].

177

178 For inversions with observation and control vectors having a high dimension, the minimum of  $J$   
 179 cannot be found analytically due to computational limitations. It can be reached iteratively with a  
 180 descent algorithm. In this case, the iterative minimization of  $J$  is based on a gradient method.  $J$  is  
 181 calculated with the forward observation operator (including the CTM) and its gradient relative to  
 182 the control parameters  $\mathbf{x}$  is provided by the adjoint of the observation operator (including the adjoint  
 183 of the CTM). The gradient is defined as:

$$184 \nabla J(\mathbf{x}) = \mathbf{B}^{-1}(\mathbf{x} - \mathbf{x}^b) + H^* \mathbf{R}^{-1}(H(\mathbf{x}) - \mathbf{y}) \text{ (Eq. 2)}$$

185 where  $H^*$  is the adjoint of the observation operator.

186

187 The high non-linearity of the chemistry for reactive species makes it difficult to use its tangent-  
 188 linear to approximate the actual observation operator, and, more generally, it makes the inversion  
 189 problem highly non-linear. Therefore, in PYVAR-CHIMERE, we use the M1QN3 limited memory  
 190 quasi-Newton minimization algorithm [Gilbert and Lemaréchal, 1989], which relies on the actual  
 191 CHIMERE non-linear model to compute  $J$  at each iteration of the minimization. As most quasi-  
 192 Newton methods, it requires an initial regularization of  $\mathbf{x}$ , the vector to be optimized, for better  
 193 efficiency. We adopt the most generally used regularization, made by minimizing in the space  
 194 defined by:

$$195 \chi = \mathbf{B}^{\frac{1}{2}}(\mathbf{x} - \mathbf{x}^b) \text{ (Eq. 3)}$$

196 instead of the control space defined by  $\mathbf{x}$ . Although more advanced regularizations can be chosen,  
 197 the minimization with  $\chi$  is preferred for its simplifying the equation to solve. In the  $\chi$ -space,  
 198 Equation 2 can be re-written as follows:

$$199 \nabla J\chi = \chi + \mathbf{B}^{\frac{1}{2}} H^* (\mathbf{R}^{-1}(H(\mathbf{x}) - \mathbf{y})) \text{ (Eq. 4)}$$

200

201 The criterion for stopping the algorithm is based on a threshold set on the ratio between the final  
 202 and initial gradient norms or on the maximum number of iterations to perform. As shown in Figure  
 203 1, the minimization algorithm repeats the forward-adjoint cycle to get an estimate close to the  
 204 optimal solution of the inversion problem for the control parameters. This approximation of the  
 205 optimal estimate is found by satisfying the convergence criteria of the minimizer with a given  
 206 reduction of the norm of the gradient of  $J$ . Nevertheless, due to the non-linearity of the problem, the  
 207 minimization may reach a local minimum only, instead of the global minimum.

208

209 Finally, the calculation of the uncertainty in the estimate of emissions from the inversion, known as  
 210 “posterior uncertainty”, is challenging in a variational inverse system [Rayner et al., 2019]. Even

though the posterior uncertainty can be explicitly written in various analytical forms, it requires the inversion of matrices that are too large to invert given the current computational resources in our variational approach. As a trade-off between computing resources and comprehensiveness, the analysis error may be evaluated by an approach based on a propagation of errors through sensitivity tests (e.g., as in Fortems-Cheiney et al., [2012]). It can also be estimated through a Monte Carlo Ensemble [Chevallier et al., 2007], implemented in PYVAR. Nevertheless, it should be noted that the cost of the Monte Carlo experiments used to derive these posterior uncertainties is huge.

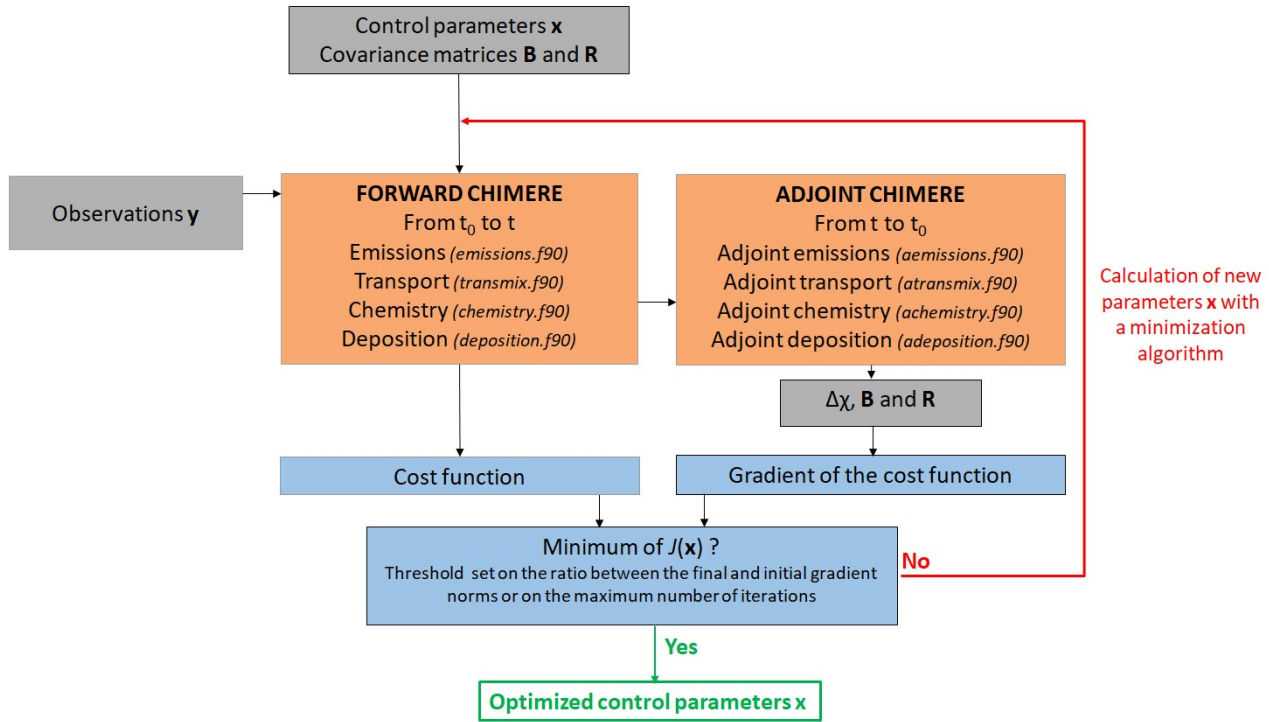


**Figure 1.** Simplified scheme of the iterative minimization in PYVAR-CHIMERE. PYVAR, CHIMERE and text sources are displayed in blue, in orange and in grey, respectively.

### 3. The PYVAR-CHIMERE configuration

#### 3.1. PYVAR adapted to CHIMERE

The PYVAR-CHIMERE inverse modeling system is based on the Bayesian variational assimilation code PYVAR [Chevallier et al. 2005] and on a previous inversion system coupled to CHIMERE [Pison et al., 2007]. PYVAR is an ensemble of Python scripts, which deals with preparing the vectors and the matrices for the inversion, drives the required Fortran codes of the transport model and computes the minimization of the cost function to solve the inversion. Previously used for global inversions with the LMDz model [e.g., Pison et al., 2009; Chevallier et al., 2010; Fortems-Cheiney et al., 2011; Yin et al., 2015; Locatelli et al., 2015; Zheng et al., 2019], PYVAR has been adapted to CHIMERE with an adjoint code without chemistry by Broquet et al. [2011]. In order to couple PYVAR to the new state-of-the-art version of CHIMERE (see Section 3.2), to include

chemistry, and to increase its modularity, flexibility and clarity, the new system described here has been developed. It includes elements of the inversion system (coded in Fortran90) of Pison et al. [2007].

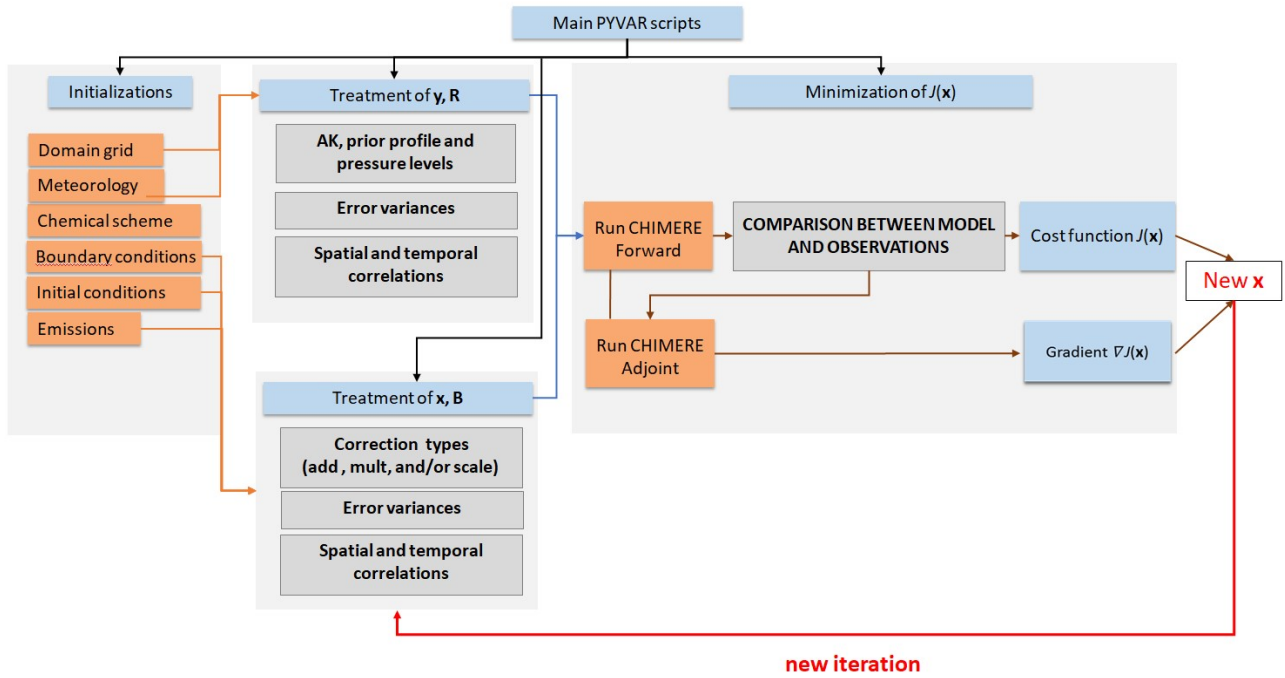
### **3.2. Development and parallelization of the adjoint and tangent-linear codes of CHIMERE**

To compute the sensitivity of simulated atmospheric concentrations to corrections to the fluxes, the adjoint of CHIMERE has been developed. Originally, the sequential adjoint was coded [Menut et al., 2000; Menut et al., 2003; Pison et al., 2007]. The adjoint has been coded by hand line by line, following the principles formulated by Talagrand [1997]. It contains exactly the same processes as the CHIMERE forward model. The code has been parallelized, which required a redesigning of the entire code, associated with a full testing scheme (see Section 3.3). Furthermore, the tangent-linear (TL) code has been developed and validated (see Section 3.3). Changes have been implemented in the forward CHIMERE code embedded in PYVAR-CHIMERE to match requirements of the studies conducted with this system. These changes have been implemented in both the adjoint and the TL codes. Compared to the CHIMERE 2013 version [Menut et al., 2013], the most important of these changes are, regarding geometry, the possibility of polar domains and the use of the coordinates of the corners of the cells instead of only the centers, allowing the use of irregular grids. Regarding transport, the non-uniform Van Leer transport scheme on the horizontal has been implemented, which is consistent with the use of irregular grids. Finally, various switches have been added to keep the system consistent for GHG studies. For example, we can avoid going into the chemistry, deposition or wet deposition routines when the focused species do not require them (e.g., no chemistry for methane or carbon dioxide at a regional scale).

PYVAR-CHIMERE is currently implemented with a full module of gaseous chemistry. As a compromise between the robustness of the method for reactive species, the time required coding the adjoint and the computational cost with a full chemical scheme, the aerosols modules of CHIMERE have not been included in the adjoint of CHIMERE yet and are therefore not available in PYVAR-CHIMERE. The development and maintenance of the adjoint means that the version used is necessarily one or two versions behind the distributed CHIMERE version (<http://www.lmd.polytechnique.fr/chimere/>). It should also be noted that PYVAR-CHIMERE only infers anthropogenic emissions at this stage. The optimization of biogenic emissions, which are linearly interpolated at the sub-hourly scale in CHIMERE, is currently under development.



268 As an example, Figure 2 presents a simplified scheme of how PYVAR scripts are used to drive this  
 269 version of CHIMERE for forward simulations and inversions using satellite observations.  
 270



271  
 272 **Figure 2.** Simplified scheme of how PYVAR scripts are used to drive CHIMERE for an inversion  
 273 using satellite observations. PYVAR, CHIMERE and text sources are displayed in blue, in orange  
 274 and in grey, respectively. “AK” refers to Averaging Kernels as detailed in Section 3.5.

275

### 276 3.3. Accuracy of tangent-linear and adjoint codes

277 Different procedures have been implemented to test the accuracy of the TL and adjoint codes. To  
 278 test the linearity of the TL, we compute a Taylor diagnostic. It consists in computing the TL at  $\mathbf{x}_0$   
 279 for given increments  $\Delta\mathbf{x}$ ,  $dH\mathbf{x}_0(\Delta\mathbf{x})$ , then the TL at  $\mathbf{x}_0$  for  $\lambda \times \Delta\mathbf{x}$  with  $\lambda$  an arbitrary small number,  
 280  $dH\mathbf{x}_0(\lambda\Delta\mathbf{x})$ . Theoretically, if the TL is well coded,  $\lambda dH\mathbf{x}_0(\Delta\mathbf{x}) = dH\mathbf{x}_0(\lambda\Delta\mathbf{x})$  by definition. In practice,  
 281 the difference must be lower than 10 times the precision of the machine on which it is run.

282

283 The adjoint code is also tested, by verifying that  $\langle H.\Delta\mathbf{x}, H.\Delta\mathbf{x} \rangle = \langle \Delta\mathbf{x}, H^T H.\Delta\mathbf{x} \rangle$  where  $H^T$  stands for  
 284 the adjoint at  $\mathbf{x}$ . What is actually computed is the ratio of the difference between the two scalar  
 285 products to the second one and the accuracy of the computation. The difference should be a few  
 286 times the precision of the machine on which it is run.

### 287 3.4. Definition of the control vector

288 The control vector is specified by the user in a text file. This file is formatted following Table 1.  
 289 The parameters to be inverted may be fluxes and/or initial conditions and/or boundary concentration  
 290 conditions, at the grid-cell resolution or for one region encompassing up to the whole domain.

291 Several types of corrections can be applied, they are defined in the code as "add", "mult" or "scale".  
 292 Both the corrections "add" and "mult" are applied to gridded control variables. For correction type  
 293 "add", the control variables are increments added to the corresponding components of the model  
 294 inputs. For correction type "mult", the control variables are scaling factors multiplying the  
 295 corresponding components of the model inputs. The difference between the two options "add" and  
 296 "mult" plays a role when inverting fluxes which can switch from positive to negative values (like  
 297 CO<sub>2</sub> natural fluxes). For type "scale", the control variables are scaling factors applied to maps  
 298 different from the maps of emissions used as prior input of the forward model: for example, activity  
 299 maps can be used and scaled to get emissions; the obtained values are then added to the  
 300 corresponding components of the model inputs. With these various types, it is possible to define the  
 301 control variables as the budgets of emissions for different regions, types of activities, and/or  
 302 processes, which can thus be directly rescaled by the inversions, similarly to what is done in  
 303 systems where the control vector is not gridded [Wang et al., 2018]).  
 304 Different simple but efficient ways of building the error covariance matrix **B** are implemented in  
 305 PYVAR-CHIMERE. The variances and correlations are defined independently. The variances are  
 306 specified by the user through standard deviation coefficient (Table 1), which can be a fixed value  
 307 ("fx") or a percentage ("pc") to define the diagonal standard deviation matrix  $\Sigma$ . For correction  
 308 types "mult" and "scale", as well as for correction type "add" with a fixed value, the value is  
 309 directly used as the standard deviation of the uncertainty in the corresponding components of the  
 310 control vector. For correction type "add" with a percentage provided, maps of standard deviation of  
 311 uncertainty are built by applying this percentage to the matching input fields (fluxes, initial  
 312 conditions, boundary conditions). The user may also provide a script to build personalized maps of  
 313 variances.  
 314  
 315 Potential correlations between uncertainties in different types of control variables, e.g. between  
 316 fluxes and boundary conditions, and correlations between uncertainties in different species, e.g.  
 317 between fluxes of CO and NO<sub>x</sub>, are not coded yet. Only correlations for a given type of control  
 318 variable and a given species are so far taken into account so that the **B** matrix is block diagonal. For  
 319 a given type of control variable and a given species (in the illustration in section 4.2.2: CO, NO or  
 320 NO<sub>2</sub> fluxes), spatial and temporal correlations can be defined using correlation lengths through time  
 321 Lt and space Ls. Those lengths are used to model temporal and/or spatial auto-correlations using an  
 322 exponentially decaying function: the correlation r between parameters and at a given location but  
 323 separated by duration  $d(x_i, x_j)$ , or at a given time but distant by  $d(x_i, x_j)$  is given by  $r(x_i, x_j) =$   
 324  $\exp\left(\frac{-d(x_i, x_j)}{L}\right)$  (Eq. 5) where  $L = L_T \vee L_S$  is the corresponding correlation length. There is no

325 correlation between uncertainties in land and ocean flux. Note that the spatial correlations are  
326 computed for each vertical level independently when dealing with control variables with vertical  
327 resolution (3D fields of fluxes when accounting for emission injection heights, or boundary/initial  
328 conditions). Vertical correlations in the uncertainties in such variables have not been coded yet.  
329 Apart from this, the system assumes that temporal correlations and spatial correlations depend on  
330 the time lag and distance but not on the specific time and location of the corresponding parameters.  
331 It also assumes that the correlation between uncertainties at different locations and different time  
332 can be derived from the product of the corresponding autocorrelation in time and space.

333 Each block of  $\mathbf{B}$  can thus be decomposed based on Kronecker products:  $\mathbf{B} = \sum C_t \otimes C_s$  (Eq. 6) where  
334  $\otimes$  is the Kronecker product,  $C_t$  and  $C_s$  are the temporal and spatial correlations, respectively. The  
335 calculations involving  $\mathbf{B}^{1/2}$  (in Eq. 3, Eq. 4) are simplified in PYVAR-CHIMERE using the Eigen-  
336 decomposition of  $C_t$  and  $C_s$ . Its square root can be calculated according to:  $C_t^{1/2} = V_{C_t} D_{C_t}^{1/2} V_{C_t}^T$  (Eq.  
337 7) (and similarly for  $C_s$ ), where  $V_{C_t}$  is the matrix with the Eigenvectors as columns, and  $D_{C_t}$  is the  
338 diagonal matrix of Eigenvalues of  $C_t$ . It is possible to chose a threshold under which the eigenvalues  
339 are truncated when computing the spatial correlations in order to save computation **time** and  
340 memory, but not when computing the temporal correlations.

Constrained species	Correction type : - Add - Mult - Scale	Spatial resolution - at the grid-cell resolution - for one region	Temporal resolution (in hours)	Input to constrain: -Fluxes -Initial conditions -Lateral Boundary conditions -Top Boundary conditions	B variance coefficient: -fx -pc	Decorrelation time (in hours)	Decorrelation length on land (in km)	Decorrelation length on sea (in km)
CO	add	0.5°x0.5°	168	Fluxes	100 %	-	-	-
CO	add	0.5°x0.5°	1	Initial conditions	15%	-	-	-
CO	add	0.5°x0.5°	168	Lateral Boundary conditions	15%	-	-	-
CO	add	0.5°x0.5°	168	Top Boundary conditions	15%	-	-	-
NO	add	0.5°x0.5°	24	Fluxes	50 %	-	50	50
NO	add	0.5°x0.5°	1	Initial conditions	15%	-	-	-
NO <sub>2</sub>	add	0.5°x0.5°	24	Fluxes	50 %	-	50	50
NO <sub>2</sub>	add	0.5°x0.5°	24	Initial conditions	15%	-	-	-

**Table 1.** Examples for the definition of the control vector and for the construction of the  $B$  matrix, as illustrated in Section 4.

### 3.5. Equivalents of the observations

During forward simulations, the equivalents of the components of  $\mathbf{y}$  (i.e, the equivalents of the individual data) are calculated by PYVAR-CHIMERE. It includes the CTM and an interpolation (see below the vertical interpolation from the model's grid to the satellite levels) or an extraction and averaging (e.g. extracting the grid cell matching the geographical coordinates of a surface station and averaging over one hour). As a compromise between technical issues such as the time required for reading/writing files, the observation operator  $H$  that generates the equivalent of the observations by the model (i.e.  $H(\mathbf{x})$ ) has been so far partly embedded in the code of CHIMERE. It makes it easier to use finer time intervals than available in the usual hourly outputs of CHIMERE to compute the required information (e.g., within the finer CTM physical time steps).

To make comparisons between simulations and satellite observations, the simulated vertical profiles are first interpolated on the satellite's levels (with a vertical interpolation on pressure levels) in CHIMERE. Then, the averaging kernels (AKs), when available, are applied to represent the vertical sensitivity of the satellite retrieval. Two types of formula, depending on the satellite observations used, have been detailed in PYVAR-CHIMERE for the use of AKs:  $C_m = AK.C_{m(o)}$  (Eq. 8) or  $C_m = x_a + AK(C_{m(o)} - x_a)$  (Eq. 9) where  $C_m$  is the modeled column, AK contains the averaging kernels,  $x_a$  is the prior profile (provided together with the AKs when relevant) and  $C_{m(o)}$  is the vertical distribution of the original model partial columns interpolated to the pressure grid of the AKs.

### 3.6. Numerical language

The PYVAR code is in Python 2.7, the CHIMERE CTM is coded in Fortran90. The CTM requires several numerical tools, compilers and libraries. The PYVAR-CHIMERE system was developed and tested using the software versions as described in Table 2.

		URL	Version
Software	Python	<a href="https://www.python.org/downloads/">https://www.python.org/downloads/</a>	2.7
	Fortran compiler ifort	<a href="https://software.intel.com/en-us/fortran-compilers">https://software.intel.com/en-us/fortran-compilers</a>	Composer-xe- 2013.2.146
Libraries or packages	UnidataNetCDF	<a href="https://www.unidata.ucar.edu/">https://www.unidata.ucar.edu/</a>	3
	Open MPI	<a href="https://www.open-mpi.org/">https://www.open-mpi.org/</a>	1.10.5
	GRIB_API	<a href="https://confluence.ecmwf.int/display/GRIB/Releases">https://confluence.ecmwf.int/display/GRIB/Releases</a>	1.14

	nco	<a href="http://nco.sourceforge.net/#Source">http://nco.sourceforge.net/#Source</a>	4.6.3
--	-----	---	-------

**Table 2.** URL addresses for the development and the use of the PYVAR-CHIMERE system and its modules.

PYVAR-CHIMERE’s computation time for one node of 10 CPUs is about 4h for 1 day of inversion (with ~10 iterations) for the European domain size of 101 (longitude) x 85 (latitude) x 17 (vertical levels) used in Section 4. The model parallelization results from a Cartesian division of the main geographical domain into several sub-domains, each one being processed by a worker process. To configure the parallel sub-domains, the user has to specify two parameters in the model parameter file: the number of sub-domains for the zonal and meridian directions. The total number of CPUs used is therefore the product of these two numbers plus one for the master process.

#### 4. Potential of PYVAR-CHIMERE for the inversion of CO and NO<sub>x</sub> emissions

The potential of the PYVAR-CHIMERE system to invert emissions of reactive species is illustrated with the inversion of CO and NO<sub>x</sub> anthropogenic emissions in Europe respectively based on MOPITT CO data and OMI NO<sub>2</sub> data. We have chosen to present an illustration of CO inversion over a 7-day window, the first week of March 2015. Considering the short lifetime of NO<sub>x</sub> of a few hours [Valin et al., 2013; Liu et al., 2016], we have chosen to present illustration of NO<sub>x</sub> inversion over a 1-day window, 19 February 2015. These particular periods have been chosen as they present a representative number of super-observations during winter, and as the emissions are high during that period. All the information required by the system to invert CO and NO<sub>x</sub> emissions is listed in Table 1.

#### 4.1. Data and model description

##### 4.1.1. Observations

We use CO data from the MOPITT instrument [Deeter et al., 2019]. MOPITT has been flown onboard the NASA EOS-Terra satellite, on a low sun-synchronous orbit that crosses the equator at 10:30 and 22:30 LST. The spatial resolution of its observations is about 22x22 km<sup>2</sup> at nadir. It has been operated nearly continuously since March 2000. MOPITT CO products are available in three variants: thermal-infrared TIR only, near-infrared NIR only and the multispectral TIR-NIR product, all containing total columns and retrieved profiles (expressed on a ten-level grid from the surface to 100 hPa). We choose to constrain CO emissions with the MOPITT surface product for our illustration. Among the different MOPITTv8 products, we choose to work with the multispectral MOPITTv8-NIR-TIR one, as it provides the highest number of observations, with a good evaluation against in situ data from NOAA stations [Deeter et al., 2019]. The MOPITTv8-NIR-TIR surface concentrations are sub-sampled into “super-observations” in order to reduce the effect of

errors that are correlated between neighboring observations: we selected the median of each subset of MOPITT data within each  $0.5^{\circ} \times 0.5^{\circ}$  grid-cell and each physical time step (about 5-10 minutes). After this screening, 8437 “super-observations” remain in the 7-day inversion (from 10667 raw observations). It is important to note that the potential of MOPITT to provide information at a high temporal resolution, up to the daily scale, is hampered by the cloud coverage (see the blanks in Figure 5b).

The observational constraint on  $\text{NO}_2$  emissions comes from the OMI QA4ECV tropospheric columns [Muller et al., 2016; Boersma et al., 2016, Boersma et al., 2017]. The Ozone Monitoring Instrument (OMI), a near-UV/Visible nadir solar backscatter spectrometer, was launched onboard EOS Aura in July 2004. It has been flown on a 705 km sun-synchronous orbit that crosses the Equator at 13:30 LT. Our data selection follows the criteria of the OMI QA4ECV data quality statement. As the spatial resolution of the OMI data is finer than that of the chosen CHIMERE model grid ( $13 \times 24 \text{ km}^2$  against  $0.5^{\circ} \times 0.5^{\circ}$ , respectively), the OMI tropospheric columns are sub-sampled into “super-observations” (median of the OMI data within the  $0.5^{\circ} \times 0.5^{\circ}$  grid-cell and each physical time step and its corresponding AK).

#### 4.1.2 CHIMERE set-up

CHIMERE is run over a  $0.5^{\circ} \times 0.5^{\circ}$  regular grid (about  $50 \times 50 \text{ km}^2$ ) and 17 vertical layers, from the surface to 200hPa (about 12km), with 8 layers within the first two kilometers. The domain includes 101 (longitude) x 85 (latitude) grid-cells ( $15.5^{\circ}\text{W}$ - $35^{\circ}\text{E}$ ;  $31.5^{\circ}\text{N}$ - $74^{\circ}\text{N}$ , see Figure 3). CHIMERE is driven by the European Centre for Medium-Range Weather Forecasts (ECMWF) meteorological forecast [Owens and Hewson, 2018]. The chemical scheme used in PYVAR-CHIMERE is MELCHIOR-2, with more than 100 reactions [Lattuat, 1997; CHIMERE 2017], including 24 for inorganic chemistry. The prior anthropogenic emissions for CO and  $\text{NO}_x$  emissions are obtained from the TNO-GHGco-v1 inventory [Super et al., 2020], the last update of the TNO-MACCII inventory [Kuenen et al., 2014]. This inventory is based on the EMEP/Centre on Emission Inventories and Projections (CEIP) official country reporting for air pollutants done in 2017. It is an inventory at  $6 \times 6 \text{ km}^2$  horizontal resolution. From the annual and national budgets, each sector is assigned to a specific proxy to quantify the spatial variability of the emissions within each country. Temporal profiles are also provided per Gridded Nomenclature For Reporting (GNFR) sector code (variations due to the month, weekday and hour). Following the Generation of European Emission Data for Episodes (GENEMIS) recommendations [Kurtenbach et al., 2001; Aumont et al., 2003],  $\text{NO}_x$  emissions are speciated as 90% of NO, 9.2% of  $\text{NO}_2$ , and 0.8% of nitrous acid ( $\text{HONO}$ ). The TNO-GHGco-v1 inventory has been aggregated to the CHIMERE grid.



438  
439  
440  
441  
442  
443  
444  
445  
446  
447  
448  
  
449  
450  
451  
452  
453  
454  
455  
456  
457  
  
458

The prior anthropogenic emissions for VOCs are obtained from the EMEP inventory [Vestreng et al., 2005; EMEP/CEIP website]. Biogenic emissions come from the Model of Emissions of Gases and Aerosols from nature (MEGAN) [Guenther et al., 2006]. Different climatological values from the LMDZ-INCA global model [Szopa et al., 2008] or from a Monitoring Atmospheric Composition and Climate (MACC) reanalysis are used to prescribe concentrations at the lateral and top boundaries and the initial atmospheric composition in the domain. Full access to and more information about the MACC reanalysis data can be obtained through the MACC-II web site (<http://www.copernicus-atmosphere.eu>). In order to ensure realistic fields of simulated CO and NO<sub>2</sub> concentrations from the beginning of the inversion period, runs have been preceded with a 10-day spin-up.

**4.1.3. CO Sensitivity to emissions and to initial and boundary conditions**

With its lifetime of about two months, CO could be strongly influenced by the initial and lateral boundary conditions prescribed in the CTM. In fact, as seen in Figure 4b, initial and boundary conditions provide a relatively flat background and the patterns which appear clearly over the background are linked to surface emissions (Figure 4a). To characterize the uncertainties in the concentration fields due to the initial and lateral boundary conditions, we performed a sensitivity test by using either climatological values from LMDZ-INCA or a MACC reanalysis: maximum relative differences in concentrations of about 15% over continental land are estimated (Figure 4c). The errors assigned to initial and boundary conditions in Section 4.2.2 are based on this sensitivity test.

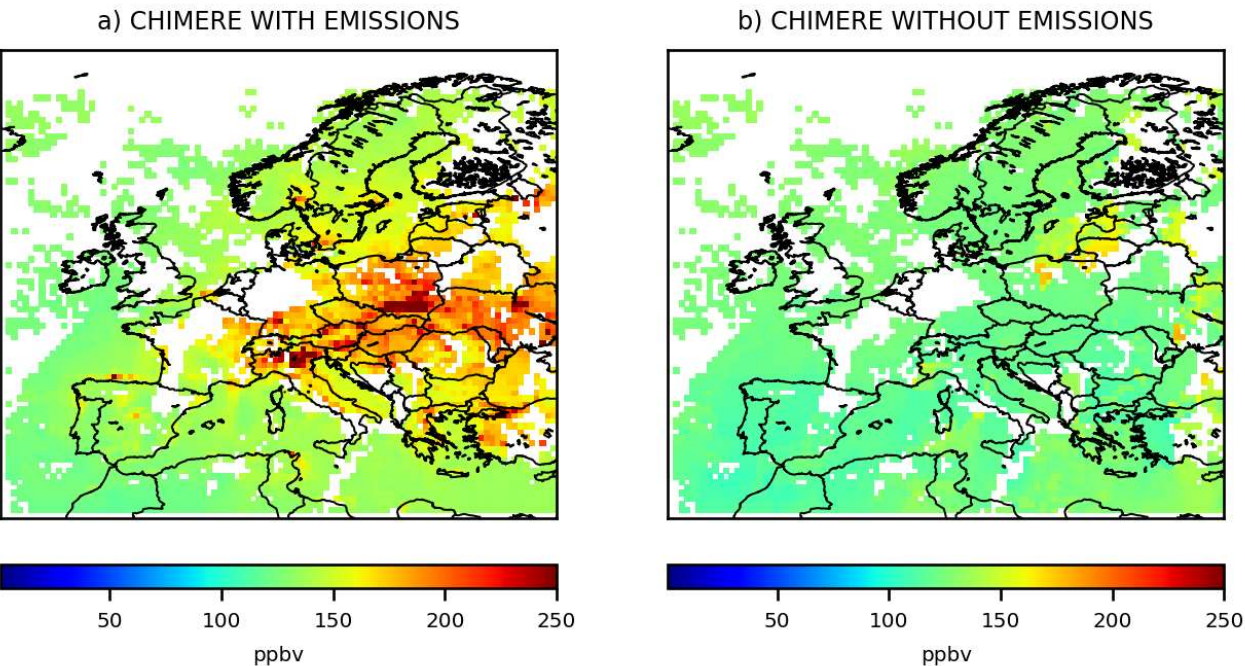


**Figure 3.** Mean CO surface concentrations from the 1<sup>st</sup> to the 7<sup>th</sup>, March 2015 simulated by CHIMERE a) with anthropogenic and biogenic emissions, and b) without emissions, in ppbv, at the 0.5°x0.5° grid-cell resolution.

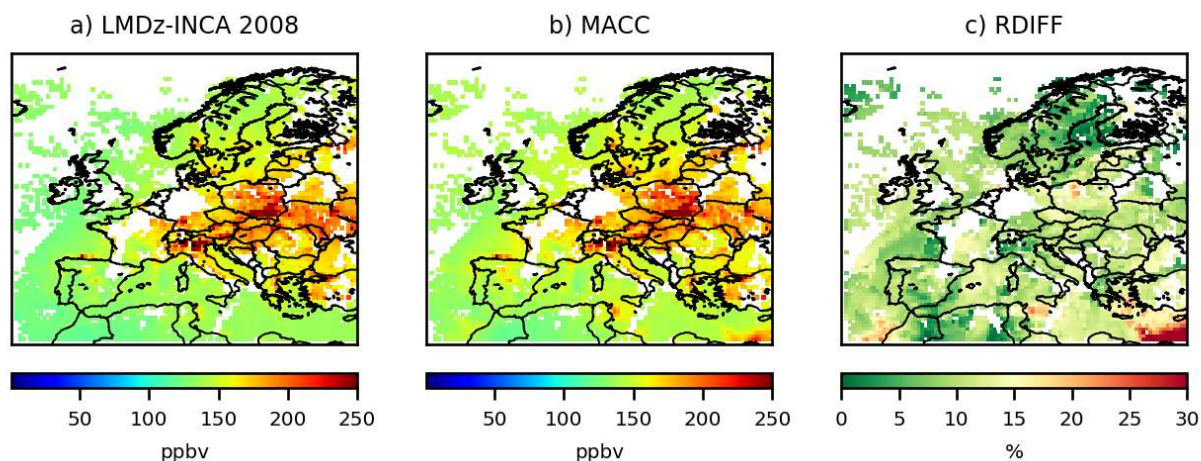


**Figure 4.** Mean CO surface concentrations from the 1<sup>st</sup> to the 7<sup>th</sup>, March 2015 simulated by CHIMERE using for initial and boundary conditions, a) the climatological values from the LMDZ-INCA global model b) the climatological values from a MACC reanalysis, in ppbv, and c) the relative differences between these two simulations, in %, at the 0.5°x0.5° grid-cell resolution.

#### 4.1.4. Comparison between CHIMERE and the observations

Large discrepancies are found between the MOPITT CO observations (Figure 5b) and the prior simulation by CHIMERE over Europe (Figure 5a). For the first week of March 2015, CO concentrations are generally under-estimated by CHIMERE, particularly over Central and Eastern Europe (excepted in the south of Poland). On the contrary, CO concentrations seem to be over-estimated over Spain and Portugal. Large discrepancies are also found between the OMI NO<sub>2</sub> super-observations and the prior simulation by PYVAR-CHIMERE (Figure 6), as already noticed by Huijnen et al. [2010], with an inter-comparison of NO<sub>2</sub> OMI-DOMINO tropospheric columns with an ensemble of European regional air quality models including CHIMERE. Over Europe, the prior simulation strongly underestimates the tropospheric columns over industrial areas (e.g., over the Netherlands and over Po Valley). These discrepancies might be due to different causes, which can all interact. A source of uncertainties is related to the observations. For example, satellite data inter-comparison studies reveal large differences between different retrievals of the same compound [Qu et al., 2020]. It can be explained by uncertainties from the CTM (e.g., through the underestimation of the atmospheric production or the underestimation of the species lifetime). It could also be explained by an underestimation of the anthropogenic emissions in the BU inventory.



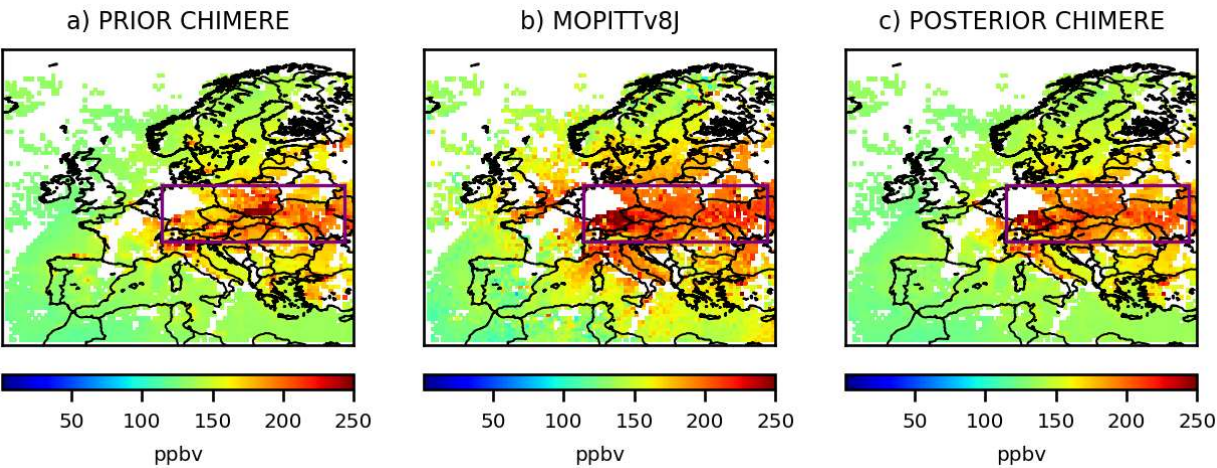


**Figure 5.** Mean CO collocated surface concentrations from the 1<sup>st</sup> to the 7<sup>th</sup>, March 2015 a) simulated by CHIMERE using the prior TNO-GHGco-v1 emissions and the climatological values from the LMDZ-INCA global model for initial and boundary conditions, b) observed by MOPITTv8-NIR-TIR and c) simulated by CHIMERE using the posterior emissions, in ppbv, at the 0.5°x0.5° grid-cell resolution. Statistics for the comparison between simulations and observations are given in Table 4 for the area in the purple box.

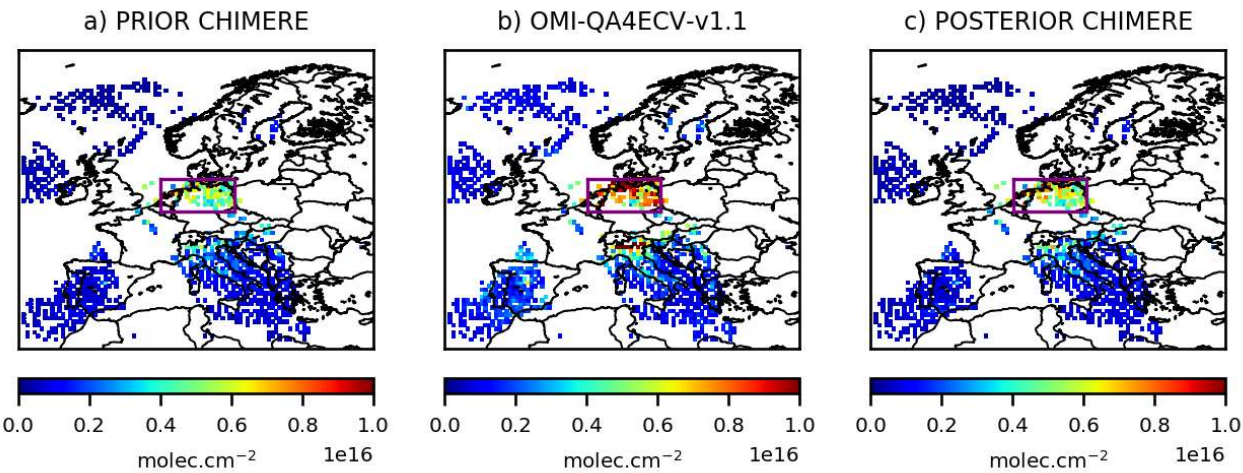


**Figure 6.** NO<sub>2</sub> collocated tropospheric columns a) simulated by CHIMERE using the prior TNO-GHGco-v1 emissions and the climatological values from the LMDZ-INCA global model for initial and boundary conditions, b) observed by OMI and c) simulated by CHIMERE using the posterior emissions, in 10<sup>16</sup> molec.cm<sup>-2</sup>, at the 0.5°x0.5° grid-cell resolution, the 19<sup>th</sup>, February 2015. Statistics for the comparison between simulations and observations are given in Table 5 for the area in the purple box.

## 4.2. Inversions

### 4.2.1. Control vector $\mathbf{x}$

For the CO inversion, the control vector  $\mathbf{x}$  contains:

- the CO anthropogenic emissions at a 7-day temporal resolution, a  $0.5^\circ \times 0.5^\circ$  (longitude, latitude) horizontal resolution, and 8 vertical levels, i.e.  $101 \times 85 \times 8$  components in  $\mathbf{x}$ ,
- the CO 3D initial conditions at a  $0.5^\circ \times 0.5^\circ$  (longitude, latitude) resolution  $\times$  17 vertical levels,
- the CO lateral and top boundary conditions at a 7-day temporal resolution, at a  $0.5^\circ \times 0.5^\circ$  (longitude, latitude) resolution, i.e.  $(2 \times 101 + 2 \times 85)$  and 17 vertical levels.

Considering its short lifetime, there is no boundary conditions for  $\text{NO}_2$ . For the  $\text{NO}_x$  inversion, the control vector  $\mathbf{x}$  contains:

- the NO and  $\text{NO}_2$  anthropogenic emissions at a 1-day temporal resolution, at a  $0.5^\circ \times 0.5^\circ$  (longitude, latitude) resolution and 8 vertical levels, i.e.  $101 \times 85 \times 8$  grid cells,
- the NO and  $\text{NO}_2$  3D initial conditions at a  $0.5^\circ \times 0.5^\circ$  (longitude, latitude) resolution and 17 vertical levels.

### 4.2.2. Covariance matrices $\mathbf{B}$ and $\mathbf{R}$

To our knowledge, there are few available studies dealing with the estimates of the uncertainties in gridded bottom-up emission inventories at the  $0.5^\circ \times 0.5^\circ$  resolution or higher. The characterization of their statistics in the inversion configuration is consequently often based on crude assumptions from the inverse modelers. **Defining the covariance matrices  $\mathbf{B}$  and  $\mathbf{R}$  is not an easy task, while incorrectly specifying these matrices has a very strong impact on the results of the inversion. Especially, the relative weights of  $\mathbf{B}$  and  $\mathbf{R}$ , and the spatial and temporal correlations in  $\mathbf{B}$  influence the degree of freedom and the structure for the adjustments attempted by the inversion in the optimization process.** Consequently, as an example for the  $\text{NO}_x$  inversion, different sensitivity tests described in Table 3 have been performed for the construction of the  $\mathbf{B}$  matrix. For both the prior NO and  $\text{NO}_2$  emissions at 1-day and  $0.5^\circ$  resolution, the prior error standard deviations are first assigned to 50% of the prior estimate of the emissions (test A), as in Sourì et al. [2020]. Sensitivity tests have also been performed with prior error standard deviations assigned to 80 and 100% of the prior estimate of the emissions (test C and test D, respectively, Figure 8).

With prior error standard deviations set at 15% of the initial conditions, the changes in initial conditions are very small (not shown) and do not affect the posterior emissions (test B, Figure 8). As indicated in Section 3.4 and in Table 1, it is possible to use correlations in  $\mathbf{B}$ , as in Broquet et al. [2011], in Broquet et al. [2013] and in Kadygrov et al. [2015]. We demonstrate the strong impact of

spatial correlations, defined by an e-folding length of 50km over land and over the sea, on our inversions results (test E, Figure 8).

Name of the sensitivity tests	Prior error standard deviations in $\mathbf{B}$		Spatial correlation in $\mathbf{B}$	Number of iterations	Reduction of the norm of the gradient of $J$
	On prior emissions	On prior initial conditions			
A	50%	-	-	4	99%
B	50%	15%	-	6	98%
C	80%	15%	-	7	97%
D	100%	15%	-	6	95%
E	50%	15%	50km	5	92%

**Table 3.** Description of the different sensitivity tests performed for the construction of the  $\mathbf{B}$  matrix for the  $\text{NO}_x$  inversion.

Even though annual CO emissions in Western Europe may be well known, with uncertainties of 6% according to Super et al., [2020], larger uncertainties could affect Eastern Europe. Moreover, large uncertainties still affect bottom-up emission inventories at the  $0.5^\circ$  resolution: spatial disaggregation of the national scale estimates to provide gridded estimates causes a significant increase in the uncertainty for CO [Super et al., 2020]. For the inversion of CO emissions, the error standard deviations assigned to the prior CO emissions at 7-day and  $0.5^\circ$  resolution are 100%. This value of 100% has already been chosen in Fortems-Cheiney et al. [2011] and in Fortems-Cheiney et al. [2012]. For this CO illustration, the covariance matrix  $\mathbf{B}$  of the prior errors is defined as diagonal (i.e. only variances in the individual control variables listed in 4.2.1 are taken into account). With such a set-up, in theory, we could obtain negative posterior emissions since the inversion system does not impose a constraint of positivity in the results. Nevertheless, even an uncertainty of 100% leads to a prior distribution mostly (>80%) on the positive side. The assimilation of data showing an increase above the background (at the edges of the domain; not shown) further drive the inversion

towards positive emissions for both CO and NO<sub>x</sub> inversions. In practice, our inversion does not lead to negative posterior emissions (Figure 7b). Spatial and temporal correlations in **B** would further limit the probability to get negative emissions locally by smoothing the posterior emissions at a spatial scale at which the “aggregated” prior uncertainty is smaller than 100%. However, a positivity constraint should be implemented in future versions of the system.

Based on the sensitivity test in Figure 4, the errors assigned to the CO lateral boundary conditions and to their initial conditions are set at 15%. As these relative errors are significantly lower than those for the emissions and as variations in the CO surface concentrations are mainly driven by emissions (Figure 3), we assume a small relative influence of the correction of initial and boundary conditions on our results. The variance of the individual observation errors in **R** is defined as the quadratic sum of the measurement error reported in the MOPITT and the OMI data sets, and of the CTM errors (including chemistry and transport errors and representativity errors) set at 20% of the retrieval values. The representativity errors could have been reduced with the choice of a finer CTM resolution (e.g., with a resolution closer to the size of the satellite pixel). Error correlations between the super-observations are neglected, so that the covariance matrix **R** of the observation errors is diagonal.

#### 4.2.3. Inversion of CO emissions

Ten iterations are needed to reduce the norm of the gradient of  $J$  by 90% with the minimization algorithm M1QN3 and obtain the increments, i.e. the corrections provided by the inversion. The prior CO emissions over Europe for the first week of March 2015 and their increments are shown in Figure 7. As expected from the large differences between the prior surface concentrations (Figure 5a) and the MOPITT observations (Figure 5b), local increments can reach more than +50% (Figure 7b). CO emissions are increased over Central and Eastern Europe, except in the south of Poland. On the contrary, CO emissions are decreased over Spain and Portugal. The analyzed concentrations are the concentrations simulated by CHIMERE with the posterior fluxes: as expected, the optimization of the fluxes improves the fit of the simulated concentrations to the observations (Figure 5c), particularly over Central and Eastern Europe. Over this area (see the purple box in Figure 5), the mean bias between the simulation and the observations has been reduced by about 27% when using the posterior emissions (mean bias of 11.6 ppbv against 15.9 ppbv with the prior emissions, Table 4). The RMSE and the standard deviation have been reduced by about 50% and the correlation has been strongly improved (0.74 when using the posterior emissions against 0.02).

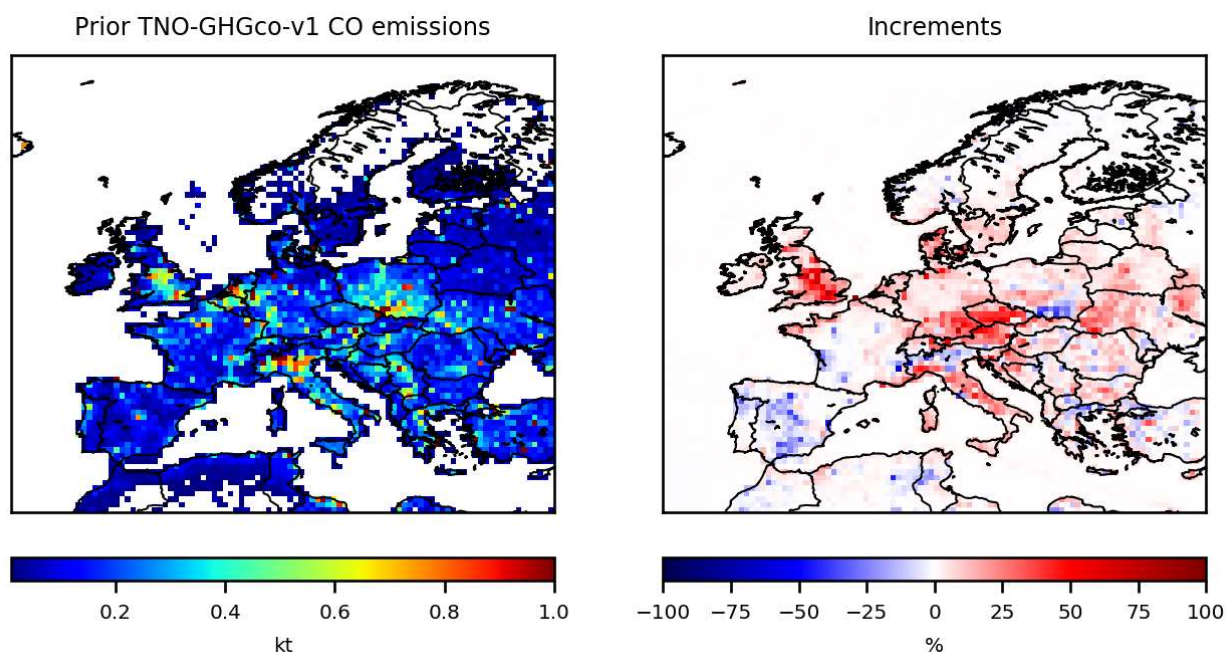


**Figure 7.** a) TNO-GHGco-v1 CO anthropogenic prior emissions, in ktCO/grid-cell and b) increments provided by the inversion with constraints from MOPITTv8-NIR-TIR from the 1<sup>st</sup> to the 7<sup>th</sup>, March 2015, in %.

prior				posterior			
MB	RMSE	STD	r	MB	RMSE	STD	r
15.88	41.95	38.82	0.02	11.58	21.14	17.69	0.74
			(p value = 0.99)				(p value = $2.08 \times 10^{-11}$ )

**Table 4.** Statistics for the comparison between simulated and observed CO surface concentrations over Central and Eastern Europe (see the area in purple in Figure 5). MB= Mean Bias, RMSE= Root Mean Square Error, STD= Standard Deviation are in ppbv. The spatial correlations  $r$  are presented with their  $p$  value.

#### 4.2.4. Inversion of NO<sub>x</sub> emissions

The prior NO<sub>x</sub> emissions and the corrections provided by the different sensitivity tests of Table 3 are shown in Figure 8. Here, we analyzed the results from inversion E. As expected from the underestimation of the prior tropospheric columns in Figure 6, local increments may be large, for example over industrial areas (e.g., over the Po Valley) and over the Netherlands, with increments of more than +50% (Figure 8b). The analyzed NO<sub>2</sub> tropospheric columns in Figure 6c are the columns simulated by CHIMERE with the NO<sub>2</sub> posterior fluxes: as expected, the optimization of the fluxes improves the fit of the simulated concentrations to the observations over the Netherlands. Over this area (see the purple box in Figure 6), where the OMI uncertainties are lower than 50%

587 (Figure 9b), the mean bias between the simulation and the observations has been reduced by about  
588 24% when using the posterior emissions (mean bias of  $1.9 \times 10^{15}$  molec.cm<sup>-2</sup> against  $2.6 \times 10^{15}$   
589 molec.cm<sup>-2</sup> with the prior emissions, Table 5, Figure 9a). The RMSE and the standard deviation  
590 have been reduced by about 7%. The correlation has not been improved.

591

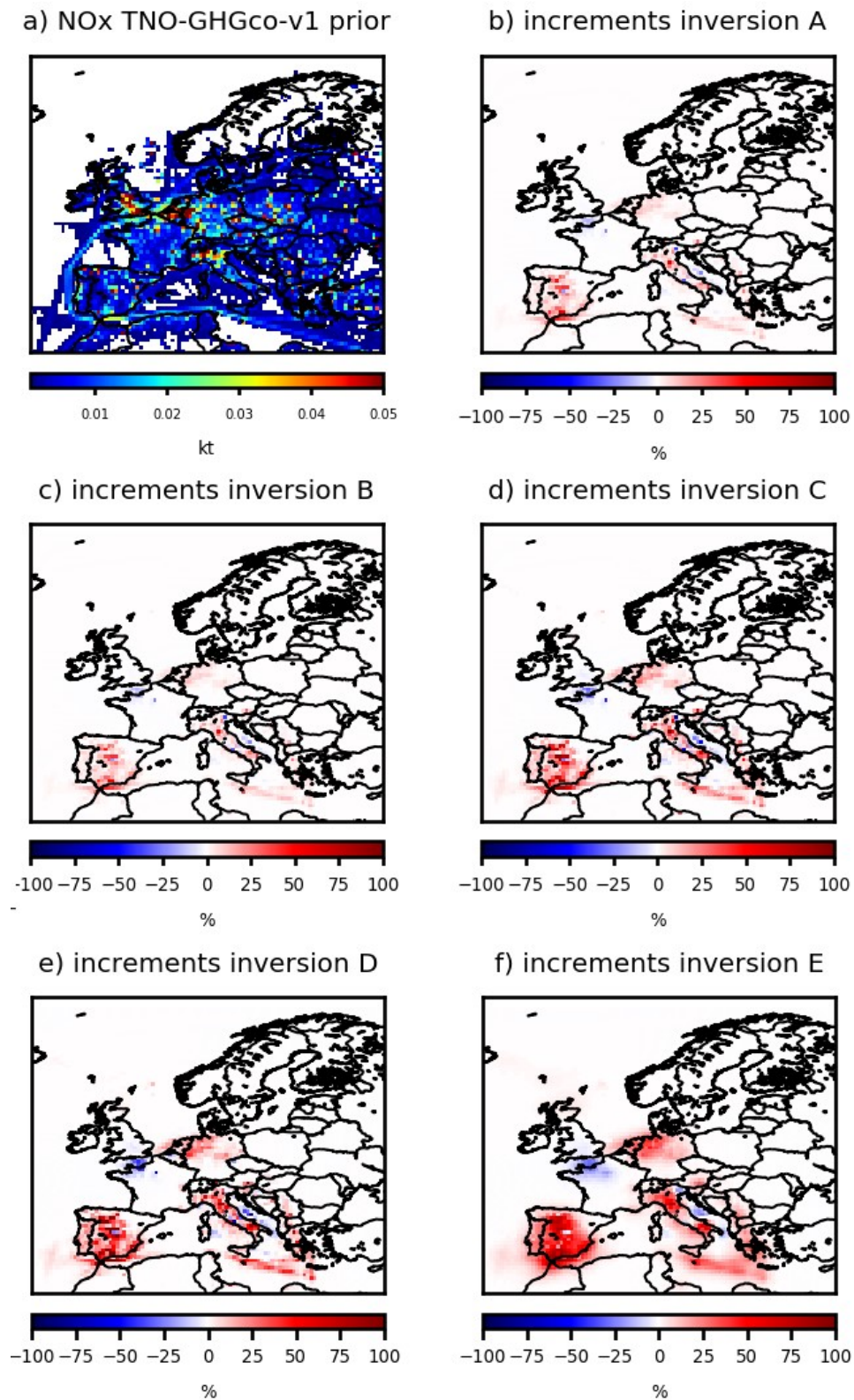
592 Even with high emission increments, the impact on the tropospheric columns is rather small. We  
593 have performed a test to explain this lack of sensitivity. We have simulated NO<sub>2</sub> columns with  
594 anthropogenic emissions increased by a factor 3 compared to the simulation in Figure 6a. The ratio  
595 between these two simulations shows strong non-linearities, blurring the multiplicative effect of our  
596 increments and explaining the lack of sensitivity (not shown). By increasing NO<sub>x</sub> anthropogenic  
597 emissions, NO<sub>2</sub> tropospheric columns can be strongly increased and can even exceed the  
598 observations values for particular pixels. NO<sub>2</sub> tropospheric columns can also be decreased or only  
599 slightly increased. On average, it tends to increase the concentrations by a factor that is much  
600 smaller than the factor of increase in the anthropogenic emissions. However, the patterns where the  
601 posterior tropospheric columns exceed the observations or, on the opposite are decreased or only  
602 slightly increased, explain why the inversion system does not attempt at increasing further the  
603 average level of the concentration (to decrease further the general bias to the observations), even  
604 though it accounts for the impact of non-linearities in the chemistry through the use of the M1QN3  
605 minimization algorithm. **We can conclude that the strong non-linearities of the NO<sub>x</sub> chemistry**  
606 **mainly explain the lack of sensitivity between NO<sub>x</sub> emissions and satellite NO<sub>2</sub> columns.**  
607 **Besides chemical effects, the lack of sensitivity could be also partly due to the contribution of**  
608 **emissions during the preceding days and the assimilation window will be widened in the near**  
609 **future.**

610

611 The posterior emissions and their uncertainties will have to be evaluated and may bring hints to the  
612 cause of the discrepancies between simulated and observed NO<sub>2</sub> tropospheric columns. The biases  
613 between OMI and simulated NO<sub>2</sub> tropospheric columns are a complex topic that is not related to our  
614 CHIMERE simulations only [Huijnen et al., 2010; Sourì et al., 2020; Elguindi et al., 2020]. Several  
615 studies have indeed already reported that strong non-linear relationships exist between NO<sub>x</sub>  
616 emissions and satellite NO<sub>2</sub> columns [Lamsal et al., 2011; Vinken et al., 2014; Miyazaki et al.,  
617 2017; Li and Wang, 2019]. This reveals that a fully comprehensive scientific study is required, by  
618 analyzing the NO<sub>x</sub> lifetime through processes such as the NO<sub>2</sub>+OH reactions and/or the reactive  
619 uptake of NO<sub>2</sub> and N<sub>2</sub>O<sub>5</sub> by aerosols [e.g. Lin et al., 2012; Stavrou et al., 2013].

620





621  
 622 **Figure 8.** a) TNO-GHGco-v1 NO<sub>x</sub> anthropogenic prior emissions, in ktNO<sub>2</sub>/grid-cell and  
 623 increments provided by the inversion b) A, c) B, d) C, e) D and f) E with constraints from OMI the  
 624 19<sup>th</sup>, February 2015, in %. The description of the different inversions is given in Table 3.  
 625

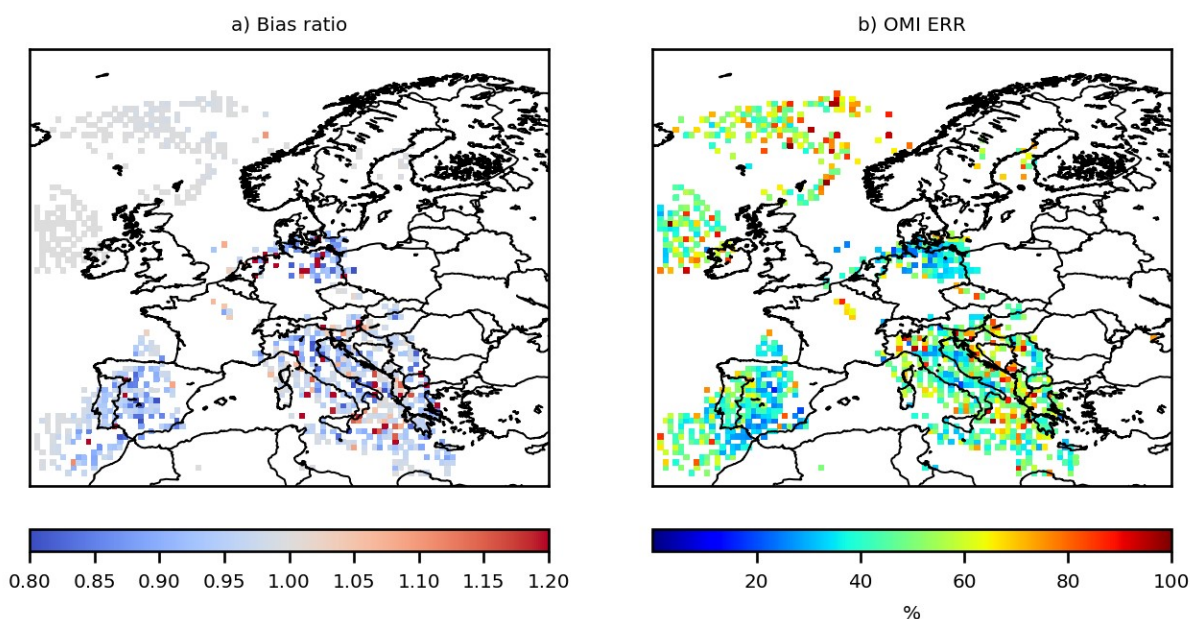


**Figure 9.** a) Bias ratio between CHIMERE simulations using the posterior emissions against prior TNO-GHGco-v1 emissions compared to the OMI-QA4ECV-v1.1 observations. All ratios lower than 1, in blue, demonstrate that posterior emissions improve the simulation compared to the prior ones. b) OMI uncertainties, in %, the 19<sup>th</sup>, February 2015.

	prior				posterior			
	MB	RMSE	STD	r	MB	RMSE	STD	r
NO <sub>2</sub>	2.6x10 <sup>15</sup>	4.0x10 <sup>15</sup>	3.0x10 <sup>15</sup>	0.008 (p=0.96)	1.9x10 <sup>15</sup>	3.74x10 <sup>15</sup>	2.9x10 <sup>15</sup>	0.01 (p=0.91)

**Table 5.** Statistics for the comparison between simulated and observed NO<sub>2</sub> tropospheric columns for the inversion E, mainly over the Netherlands (see the area in purple in Figure 6). MB= Mean Bias, RMSE= Root Mean Square Error, STD= Standard Deviation are in molec<sub>m</sub>.cm<sup>-2</sup>. The spatial correlations *r* are presented with their *p* value.

## 5. Conclusion/Discussion

This paper presents the Bayesian variational inverse system PYVAR-CHIMERE, which has been adapted to the inversion of reactive species such as CO and NO<sub>x</sub>, taking advantage of the previous developments for long-lived species such as CO<sub>2</sub> [Broquet et al., 2011] and CH<sub>4</sub> [Pison et al., 2018]. We show the potential of PYVAR-CHIMERE, with inversions for CO and NO<sub>x</sub> illustrated over Europe. PYVAR-CHIMERE will now be used to infer CO and NO<sub>x</sub> emissions over long periods, e.g. first for a whole season or year and then for the recent decade 2005-2015 in the framework of the H2020 VERIFY project over Europe, and in the framework of the ANR PolEASIA project over China, to quantify their trend and their spatio-temporal variability. Nevertheless, as we have reported strong non-linear relationships between NO<sub>x</sub> emissions and



642 satellite NO<sub>2</sub> columns, a fully comprehensive scientific study is required, by analyzing the NO<sub>x</sub>  
643 lifetime through processes such as the NO<sub>2</sub>+OH reactions and/or the reactive uptake of NO<sub>2</sub> and  
644 N<sub>2</sub>O<sub>5</sub> by aerosols [e.g. Lin et al., 2012; Stavrou et al., 2013]. Biogenic emissions will be also  
645 further studied to better understand the relationship between NO<sub>x</sub> emissions and NO<sub>2</sub> spaceborne  
646 columns.

647

648 The PYVAR-CHIMERE system can handle any large number of both control parameters and  
649 observations. It will be able to cope with the dramatic increase in the number of data in the near  
650 future with, for example, the high-resolution imaging (pixel of 7x3.5 km<sup>2</sup>) of the new Sentinel-  
651 5P/TROPOMI program, launched in October 2017. These new space missions with high-resolution  
652 imaging have indeed the ambition to monitor atmospheric chemical composition for the  
653 quantification of anthropogenic emissions. Moreover, a step forward in the joint assimilation of co-  
654 emitted pollutants will be possible with the PYVAR-CHIMERE system and the availability of  
655 TROPOMI co-localized images of CO and NO<sub>2</sub>. This should improve the consistency of the  
656 inversion results and can be used to inform inventory compilers, and subsequently improve  
657 emission inventories. Moreover, this development will help in further understanding air quality  
658 problems and addressing air quality related emissions at the national to subnational scales.

659

#### 660 **Author Contribution**

661 All authors have contributed to the manuscript writing (main authors: AFC, GB, IP and GD) and to  
662 the development of the present version of the PYVAR-CHIMERE system (main developer: IP). IP  
663 and GD have parallelized the adjoint version from Menut et al., [2000], Menut et al., [2003] and  
664 Pison et al., [2007]. IP has complemented the adjoint of new parameterizations since the CHIMERE  
665 release in 2011 and the tangent-linear model.

666

#### 667 **Code and Data Availability**

668 OMI QA4ECV NO<sub>2</sub> product can be found here: <http://temis.nl/qa4ecv/no2.html>.

669 MOPITTv8-NIR-TIR CO product can be found here: <ftp://15ftl01.larc.nasa.gov/MOPITT/>

670 The CHIMERE code is available here: [www.lmd.polytechnique.fr/chimere/](http://www.lmd.polytechnique.fr/chimere/).

671

672 The associated documentation of PYVAR-CHIMERE is available on the website  
673 <https://pyvar.lsce.ipsl.fr/doku.php/3chimere:headpage>. The documentation includes a whole  
674 description of PYVAR-CHIMERE and several tutorials on how to run a first PYVAR-CHIMERE  
675 simulation or how to run an inversion.

676

#### 677 **Competing interests**

678 The authors declare that they have no conflict of interest.

679

#### 680 **Acknowledgements**

681 We acknowledge L. Menut and C. Schmechtig for their contributions to the development work on  
682 the adjoint code of CHIMERE and its parallelization. We acknowledge the TNO team (H.A. Denier

van der Gon, J. Kuenen, S. Dellaert, S. Jonkers, A. Visschedijk, et al.) for providing NO<sub>x</sub> and CO emissions over Europe. We also acknowledge the free use of tropospheric NO<sub>2</sub> column data from the OMI sensor from <http://temis.nl/qa4ecv/no2.html> and the free use of CO surface concentrations from the MOPITT sensor from <ftp://15ftl01.larc.nasa.gov/MOPITT/>. For this study, A. Fortems-Cheiney was funded by the French Space Agency-Centre National d'Etudes Spatiales CNES and by the H2020 VERIFY project, funded by the European Commission Horizon 2020 research and innovation programme, under agreement number 776810. L. Costantino was funded by the PolEASIA ANR project under the allocation ANR-15-CE04-0005. This work was granted access to the HPC resources of TGCC under the allocations A0050107232 and A0070102201 made by GENCI. Finally, we wish to thank F. Marabelle (LSCE) and his team for computer support.

## References

Aumont, B., Chervier, F., and Laval, S.: Contribution of HONO sources to the NO<sub>x</sub>/HO<sub>x</sub>/O<sub>3</sub> chemistry in the polluted boundary layer. *Atmospheric Environment*, 37(4):487 – 498, 2003.

Belikov, D. A., Maksyutov, S., Yaremchuk, A., Ganshin, A., Kaminski, T., Blessing, S., Sasakawa, M., Gomez-Pelaez, A. J., and Starchenko, A.: Adjoint of the global Eulerian–Lagrangian coupled atmospheric transport model (A-GELCA v1.0): development and validation, *Geosci. Model Dev.*, 9, 749–764, <https://doi.org/10.5194/gmd-9-749-2016>, 2016.

Boersma, K. F., Vinken, G. C. M., and Eskes, H. J.: Representativeness errors in comparing chemistry transport and chemistry climate models with satellite UV–Vis tropospheric column retrievals, *Geosci. Model Dev.*, 9, 875–898, <https://doi.org/10.5194/gmd-9-875-2016>, 2016.

Boersma, K. F., Eskes, H., Richter, A., De Smedt, I., Lorente, A., Beirle, S., Van Geffen, J., Peters, E., Van Roozendaal, M. and Wagner, T.: QA4ECV NO<sub>2</sub> tropospheric and stratospheric vertical column data from OMI (Version 1.1) [Data set], Royal Netherlands Meteorological Institute (KNMI), <http://doi.org/10.21944/qa4ecv-no2-omi-v1.1>, 2017.

Bousquet, P., P. Ciais, P. Peylin, M. Ramonet, and P. Monfray: Inverse modeling of annual atmospheric CO<sub>2</sub> sources and sinks: 1. Method and control inversion, *J. Geophys. Res.*, 104(D21), 26,161 – 26,178, doi:10.1029/1999JD900342, 1999.

Broquet, G., Chevallier, F., Rayner, P., Aulagnier, C., Pison, I., Ramonet, M., Schmidt, M., Vermeulen, A. T., and Ciais, P.: A European summertime CO<sub>2</sub> biogenic flux inversion at mesoscale from continuous in situ mixing ratio measurements, *J. Geophys. Res.*, 116, D23303, doi:10.1029/2011JD016202, 2011.

Broquet, G., Chevallier, F., Bréon, F.-M., Kadyrov, N., Alemanno, M., Apadula, F., Hammer, S., Haszpra, L., Meinhardt, F., Morguá, J. A., Necki, J., Piacentino, S., Ramonet, M., Schmidt, M., Thompson, R. L., Vermeulen, A. T., Yver, C., and Ciais, P.: Regional inversion of CO<sub>2</sub> ecosystem fluxes from atmospheric measurements: reliability of the uncertainty estimates, *Atmos. Chem. Phys.*, 13, 9039–9056, <https://doi.org/10.5194/acp-13-9039-2013>, 2013.

Chevallier, F., M. Fisher, P. Peylin, S. Serrar, P. Bousquet, F.-M. Bréon, A. Chédin, and P. Ciais: Inferring CO<sub>2</sub> sources and sinks from satellite observations: method and application to TOVS data, *J. Geophys. Res.*, 110, D24309, [doi:10.1029/2005JD006390](https://doi.org/10.1029/2005JD006390), 2005.

Chevallier, F., F.-M. Bréon, and P. J. Rayner: The contribution of the Orbiting Carbon Observatory to the estimation of CO<sub>2</sub> sources and sinks: Theoretical study in a variational data assimilation framework. *J. Geophys. Res.*, 112, D09307, [doi:10.1029/2006JD007375](https://doi.org/10.1029/2006JD007375), 2007.

Chevallier, F., Ciais, P., Conway, T. J., Aalto, T., Anderson, B. E., Bousquet, P., Brunke, E. G., Ciattaglia, L., Esaki, Y., Fröhlich, M., Gomez, A., Gomez-Pelaez, A. J., Haszpra, L., Krummel, P. B., Langenfelds, R. L., Leuenberger, M., Machida, T., Maignan, F., Matsueda, H., Morguí, J. A., Mukai, H., Nakazawa, T., Peylin, P., Ramonet, M., Rivier, L., Sawa, Y., Schmidt, M., Steele, L. P., Vay, S. A., Vermeulen, A. T., Wofsy, S., and Worthy, D.: CO<sub>2</sub> surface fluxes at grid point scale estimated from a global 21 year reanalysis of atmospheric measurements, *J. Geophys. Res.*, 115, 1–17, <https://doi.org/10.1029/2010jd013887>, 2010.

Ciarelli, G., Theobald, M. R., Vivanco, M. G., Beekmann, M., Aas, W., Andersson, C., Bergstrom, R., Manders-Groot, A., Couvidat, F., Mircea, M., Tsyro, S., Fagerli, H., Mar, K., Raffort, V., Roustan, Y., Pay, M.-T., Schaap, M., Kranenburg, R., Adani, M., Briganti, G., Cappelletti, A., D'Isidoro, M., Cuvelier, C., Cholakian, A., Bessagnet, B., Wind, P., and Colette, A.: Trends of inorganic and organic aerosols and precursor gases in Europe: insights from the EURODELTA multi-model experiment over the 1990-2010 period, *Geosci. Model Dev.*, 12, 4923-4954, <https://doi.org/10.5194/gmd-12-4923-2019>, 2019.

CHIMERE documentation, <https://www.lmd.polytechnique.fr/chimere/docs/CHIMEREdoc2017.pdf>, Last update of this documentation: June 8, 2017, 2017.

Deeter, M. N., Edwards, D. P., Francis, G. L., Gille, J. C., Mao, D., Martínez-Alonso, S., Worden, H. M., Ziskin, D., and Andreae, M. O.: Radiance-based retrieval bias mitigation for the MOPITT instrument: the version 8 product, *Atmos. Meas. Tech.*, 12, 4561–4580, <https://doi.org/10.5194/amt-12-4561-2019>, 2019.

Ding, J., Miyazaki, K., van der A, R. J., Mijling, B., Kurokawa, J.-I., Cho, S., Janssens-Maenhout, G., Zhang, Q., Liu, F., and Levelt, P. F.: Intercomparison of NO<sub>x</sub> emission inventories over East Asia, *Atmos. Chem. Phys.*, 17, 10125-10141, <https://doi.org/10.5194/acp-17-10125-2017>, 2017.

EEA, Air quality in Europe - 2018 report, 12/2018, <https://www.eea.europa.eu/publications/air-quality-in-europe-2018>.

Elbern, H., Strunk, A., Schmidt, H., and Talagrand, O.: Emission rate and chemical state estimation by 4-dimensional variational inversion, *Atmos. Chem. Phys.*, 7, 3749-3769, <https://doi.org/10.5194/acp-7-3749-2007>, 2007.

Elguindi, N., Granier, C., Stavrakou, T., Darras, S., Bauwens, M., Cao, H., et al.: Intercomparison of magnitudes and trends in anthropogenic surface emissions from bottom-up inventories, top-down estimates, and emission scenarios. *Earth's Future*, 8, e2020EF001520. <https://doi.org/10.1029/2020EF001520>, 2020.

EMEP/EEA air pollutant emission inventory guidebook, 2016.

EMEP/CEIP,

[https://ceip.at/ms/ceip\\_home1/ceip\\_home/webdab\\_emepdatabase/emissions\\_emepmodels/](https://ceip.at/ms/ceip_home1/ceip_home/webdab_emepdatabase/emissions_emepmodels/)

- de Foy, B., Lu, Z. and Streets, D.G.: Satellite NO<sub>2</sub> retrievals suggest China has exceeded its NO<sub>x</sub> reduction goals from the twelfth Five-Year Plan, *Nature Scientific Reports*, 6:35912, 2016.
- Fortems-Cheiney, A., et al: Ten years of CO emissions as seen from MOPITT, *Journal of Geophysical Research*, 116, D5, <https://doi.org/10.1029/2010JD014416>, 2011.
- Fortems-Cheiney, A., Chevallier, F., Pison, I., Bousquet, P., Saunois, M., Szopa, S., Cressot, C., Kurosu, T. P., Chance, K., and Fried, A.: The formaldehyde budget as seen by a global-scale multi-constraint and multi-species inversion system, *Atmos. Chem. Phys.*, 12, 6699–6721, <https://doi.org/10.5194/acp-12-6699-2012>, 2012.
- Gilbert, J., and C. Lemaréchal (1989), Some numerical experiments with variable storage quasi Newton algorithms, *Math. Program.*, 45, 407–435.
- Guenther, A., Karl, T., Harley, P., Wiedinmyer, C., Palmer, P. I., and Geron, C.: Estimates of global terrestrial isoprene emissions using MEGAN (Model of Emissions of Gases and Aerosols from Nature), *Atmos. Chem. Phys.*, 6, 3181–3210, <https://doi.org/10.5194/acp-6-3181-2006>, 2006.
- Hakami, A., Henze, D. K., Seinfeld, J. H., Singh, K., Sandu, A., Kim, S., Byun, D., and Li, Q.: The adjoint of CMAQ, *Environ. Sci. Technol.*, 41, 7807–7817, <https://doi.org/10.1021/es070944p>, 2007.
- Hein, R., et coll.: An inverse modeling approach to investigate the global atmospheric methane cycle, *Global. Biogeochem. Cycles*, 11, 43-76, 1997.
- Henze, D. K., Hakami, A., and Seinfeld, J. H.: Development of the adjoint of GEOS-Chem, *Atmos. Chem. Phys.*, 7, 2413–2433, <https://doi.org/10.5194/acp-7-2413-2007>, 2007.
- Huijnen, V., Eskes, H. J., Poupkou, A., Elbern, H., Boersma, K. F., Foret, G., Sofiev, M., Valdebenito, A., Flemming, J., Stein, O., Gross, A., Robertson, L., D'Isidoro, M., Kioutsioukis, I., Friese, E., Amstrup, B., Bergstrom, R., Strunk, A., Vira, J., Zyryanov, D., Maurizi, A., Melas, D., Peuch, V.-H., and Zerefos, C.: Comparison of OMI NO<sub>2</sub> tropospheric columns with an ensemble of global and European regional air quality models, *Atmos. Chem. Phys.*, 10, 3273–3296, <https://doi.org/10.5194/acp-10-3273-2010>, 2010.
- Hooghiemstra, P. B., Krol, M. C., Bergamaschi, P., de Laat, A. T. J., van der Werf, G. R., Novelli, P.C., Deeter, M. N., Aben, I., and Rockmann, T.: Comparing optimized CO emission estimates using MOPITT or NOAA surface network observations, *J. Geophys. Res.*, 117, D06309, [doi:10.1029/2011JD017043](https://doi.org/10.1029/2011JD017043), 2012.
- Kadyrov, N., Broquet, G., Chevallier, F., Rivier, L., Gerbig, C., and Ciais, P.: On the potential of the ICOS atmospheric CO<sub>2</sub> measurement network for estimating the biogenic CO<sub>2</sub> budget of Europe, *Atmos. Chem. Phys.*, 15, 12765–12787, <https://doi.org/10.5194/acp-15-12765-2015>, 2015.
- Kononov, I. B. et coll.: Inverse modelling of the spatial distribution of NO emissions on a continental scale using satellite data, *Atmos. Chem. Phys.*, 6, 1747-1770, [doi:10.5194/acp-6-1747-2006](https://doi.org/10.5194/acp-6-1747-2006), 2006.
- Kononov, I. B., Beekmann, M., Burrows, J. P., and Richter, A.: Satellite measurement based estimates of decadal changes in European nitrogen oxides emissions, *Atmos. Chem. Phys.*, 8, 2623-2641, [doi:10.5194/acp-8-2623-2008](https://doi.org/10.5194/acp-8-2623-2008), 2008.

- Konovalov, I. B., Beekmann, M., Richter, A., Burrows, J. P., and Hilboll, A.: Multi-annual changes of NO<sub>x</sub> emissions in megacity regions: nonlinear trend analysis of satellite measurement based estimates, *Atmos. Chem. Phys.*, 10, 8481-8498, doi:10.5194/acp-10-8481-2010, 2010.
- Koohkan, M. R., Bocquet, M., Roustan, Y., Kim, Y., and Seigneur, C.: Estimation of volatile organic compound emissions for Europe using data assimilation, *Atmos. Chem. Phys.*, 13, 5887-5905, <https://doi.org/10.5194/acp-13-5887-2013>, 2013.
- Krol, M. C., Meirink, J. F., Bergamaschi, P., Mak, J. E., Lowe, D., Jöckel, P., Houweling, S., and Röckmann, T.: What can 14CO measurements tell us about OH?, *Atmospheric chemistry and physics*, 8, 5033–5044, 2008.
- Kuenen, J. J. P., Visschedijk, A. J. H., Jozwicka, M., and Denier van der Gon, H. A. C.: TNO-MACC II emission inventory; a multi-year (2003–2009) consistent high-resolution European emission inventory for air quality modelling, *Atmos. Chem. Phys.*, 14, 10963-10976, <https://doi.org/10.5194/acp-14-10963-2014>, 2014.
- Kurokawa, J., Ohara, T., Morikawa, T., Hanayama, S., Janssens-Maenhout, G., Fukui, T., Kawashima, K., and Akimoto, H.: Emissions of air pollutants and greenhouse gases over Asian regions during 2000–2008: Regional Emission inventory in ASia (REAS) version 2, *Atmos. Chem. Phys.*, 13, 11019-11058, doi:10.5194/acp-13-11019-2013, 2013.
- Kurtenbach, R., Becker, K., Gomes, J., Kleffmann, J., Lžrzer, J., Spittler, M., Wiesen, P., Ackermann, R., Geyer, A., and Platt, U.: Investigations of emissions and heterogeneous formation of HONO in a road traffic tunnel. *Atmospheric Environment*, 35(20):9506 – 9517. 3385D3394, 2001.
- Lamsal, L. N., Martin, R. V., Padmanabhan, A., van Donkelaar, A., Zhang, Q., Sioris, C. E., Chance, K., Kurosu, T. P., and Newchurch, M. J.: Application of satellite observations for timely updates to global anthropogenic NO<sub>x</sub> emission inventories, *Geophys. Res. Lett.*, 38, L05810, doi:[10.1029/2010GL046476](https://doi.org/10.1029/2010GL046476), 2011.
- Lattuati, M., Impact des émissions européennes sur le bilan de l'ozone troposphérique a l'interface de l'europe et de l'atlantique nord : apport de la modélisation lagrangienne et des mesures en altitude, Ph.D. thesis, Université Paris VI, 1997.
- Lelieveld, J., Klingmüller, K., Pozzer, A., Pöschl, U., Fnais, M., Daiber, A., Münzel, T.; Cardiovascular disease burden from ambient air pollution in Europe reassessed using novel hazard ratio functions, *European Heart Journal*, , ehz135, <https://doi.org/10.1093/eurheartj/ehz135>, 2019.
- Li, J. and Wang, Y.: Inferring the anthropogenic NO<sub>x</sub> emission trend over the United States during 2003–2017 from satellite observations: was there a flattening of the emission trend after the Great Recession?, *Atmos. Chem. Phys.*, 19, 15339–15352, <https://doi.org/10.5194/acp-19-15339-2019>, 2019.
- Lin, J.-T., McElroy, M. B., and Boersma, K. F.: Constraint of anthropogenic NO<sub>x</sub> emissions in China from different sectors: a new methodology using multiple satellite retrievals, *Atmos. Chem. Phys.*, 10, 63-78, doi:10.5194/acp-10-63-2010, 2010.



- Lin, J.-T., Liu, Z., Zhang, Q., Liu, H., Mao, J., and Zhuang, G.: Modeling uncertainties for tropospheric nitrogen dioxide columns affecting satellite-based inverse modeling of nitrogen oxides emissions, *Atmos. Chem. Phys.*, 12, 12255–12275, <https://doi.org/10.5194/acp-12-12255-2012>, 2012.
- Liu, F., Beirle, S., Zhang, Q., Dörner, S., He, K., and Wagner, T.: NO<sub>x</sub> lifetimes and emissions of cities and power plants in polluted background estimated by satellite observations, *Atmos. Chem. Phys.*, 16, 5283–5298, <https://doi.org/10.5194/acp-16-5283-2016>, 2016.
- Locatelli, R., Bousquet, P., Saunio, M., Chevallier, F., and Cressot, C.: Sensitivity of the recent methane budget to LMDz sub-grid-scale physical parameterizations, *Atmos. Chem. Phys.*, 15, 9765–9780, <https://doi.org/10.5194/acp-15-9765-2015>, 2015.
- Mailler S., L. Menut, D. Khvorostyanov, M. Valari, F. Couvidat, G. Siour, S. Turquety, R. Briant, P. Tuccella, B. Bessagnet, A. Colette, L. Letinois, and F. Meleux, CHIMERE-2017: from urban to hemispheric chemistry-transport modeling ,*Geosci. Model Dev.*, 10, 2397–2423, <https://doi.org/10.5194/gmd-10-2397-2017>, 2017.
- Menut, L., R. Vautard, M. Beekmann, and C. Honoré: Sensitivity of photochemical pollution using the adjoint of a simplified chemistry-transport model, *J. Geophys. Res.*, 105, 15,379–15,402, 2000.
- Menut L.: Adjoint modelling for atmospheric pollution processes sensitivity at regional scale during the ESQUIF IOP2, *Journal of Geophysical Research - Atmospheres*, 108, D17, <https://doi.org/10.1029/2002JD002549>, 2003.
- Menut, L., Goussebaile, A., Bessagnet, B., Khvorostyanov, D., and Ung, A.: Impact of realistic hourly emissions profiles on air pollutants concentrations modelled with CHIMERE, *Atmospheric Environment*, 49, 233–244, doi:10.1016/j.atmosenv.2011.11.057, 2012.
- Menut, L., Bessagnet, B., Khvorostyanov, D., Beekmann, M., Blond, N., Colette, A., Coll, I., Curci, G., Foret, G., Hodzic, A., Mailler, S., Meleux, F., Monge, J.-L., Pison, I., Siour, G., Turquety, S., Valari, M., Vautard, R., and Vivanco, M. G.: CHIMERE 2013: a model for regional atmospheric composition modelling, *Geosci. Model Dev.*, 6, 981–1028, doi:10.5194/gmd-6-981-2013, 2013.
- Menut, L., Bessagnet, B., Siour, G., Mailler, S., Pennel, R. and Cholakian, A. : Impact of lockdown measures to combat Covid-19 on air quality over western Europe, *Science of The Total Environment*, 741, <https://doi.org/10.1016/j.scitotenv.2020.140426>, 2020.
- Mijling, B., and R. J. van der A: Using daily satellite observations to estimate emissions of short-lived air pollutants on a mesoscopic scale, *J. Geophys. Res.*, 117, D17302, doi:10.1029/2012JD017817, 2012.
- Mijling, B., et al., Regional nitrogen oxides emission trends in East Asia observed from space, *Atmos. Chem. Phys.*, 3, 12003, 2013.
- Miyazaki, K., Eskes, H., Sudo, K., Boersma, K. F., Bowman, K., and Kanaya, Y.: Decadal changes in global surface NO<sub>x</sub> emissions from multi-constituent satellite data assimilation, *Atmos. Chem. Phys.*, 17, 807–837, <https://doi.org/10.5194/acp-17-807-2017>, 2017.

- Muller, J.-P., Kharbouche, S., Gobron, N., Scanlon, T., Govaerts, Y., Danne, O., Schultz, J., Lattanzio, A., Peters, E., De Smedt, I., Beirle, S., Lorente, A., Coheur, P. F., George, M., Wagner, T., Hilboll, A., Richter, A., Van Roozendael, M., and Boersma, K. F.: Recommendations (scientific) on best practices for retrievals for Land and Atmosphere ECVs (QA4ECV Deliverable 4.2 version 1.0), 186 pp., available at: <http://www.qa4ecv.eu/sites/default/files/D4.2.pdf> (last access: 12 April 2018), 2016.
- Owens, R. G. and Hewson, T.: ECMWF Forecast User Guide, Reading, <https://doi.org/10.21957/m1cs7h>, <https://software.ecmwf.int/wiki/display/FUG/Forecast+User+Guide>, 2018.
- Pétron, G., Granier, C., Khattatov, B., Lamarque, J.F., Yudin, V., Muller, J.F. and Gille, J.: Inverse modeling of carbon monoxide surface emissions using CMDL networks observations, *J. Geophys. Res.*, 107, D24, 2002.
- Pison, I., Menut, L., and Bergametti, G.: Inverse modeling of surface NO<sub>x</sub> anthropogenic emission fluxes in the Paris area during the ESQUIF campaign, *J. Geophys. Res. Atmos.*, 112, D24302, doi:10.1029/2007JD008871, 2007.
- Pison, I., Bousquet, P., Chevallier, F., Szopa, S., and Hauglustaine, D.: Multi-species inversion of CH<sub>4</sub>, CO and H<sub>2</sub> emissions from surface measurements, *Atmospheric Chemistry and Physics*, 9, 5281–5297, 2009.
- Pison, I., Berchet, A., Saunois, M., Bousquet, P., Broquet, G., Conil, S., Delmotte, M., Ganesan, A., Laurent, O., Martin, D., O'Doherty, S., Ramonet, M., Spain, T. G., Vermeulen, A., and Yver Kwok, C.: How a European network may help with estimating methane emissions on the French national scale, *Atmos. Chem. Phys.*, 18, 3779–3798, <https://doi.org/10.5194/acp-18-3779-2018>, 2018.
- Qu, Z., Henze, D. K., Cooper, O. R., and Neu, J. L.: Improving NO<sub>2</sub> and ozone simulations through global NO<sub>x</sub> emission inversions, *Atmos. Chem. Phys. Discuss.*, <https://doi.org/10.5194/acp-2020-307>, in review, 2020.
- Rayner, P. J., Michalak, A. M., and Chevallier, F.: Fundamentals of data assimilation applied to biogeochemistry, *Atmos. Chem. Phys.*, 19, 13911–13932, <https://doi.org/10.5194/acp-19-13911-2019>, 2019.
- Souri, A. H., Nowlan, C. R., González Abad, G., Zhu, L., Blake, D. R., Fried, A., Weinheimer, A. J., Wisthaler, A., Woo, J.-H., Zhang, Q., Chan Miller, C. E., Liu, X., and Chance, K.: An inversion of NO<sub>x</sub> and non-methane volatile organic compound (NMVOC) emissions using satellite observations during the KORUS-AQ campaign and implications for surface ozone over East Asia, *Atmos. Chem. Phys.*, 20, 9837–9854, <https://doi.org/10.5194/acp-20-9837-2020>, 2020.
- Stavrakou, T. and J.-F. Müller: Grid-based versus big region approach for inverting CO emissions using Measurement of Pollution in the Troposphere (MOPITT) data, *Journal of Geophysical Research: Atmospheres*, 111, D15, 2006.
- Stavrakou, T., Muller, J.-F., Boersma, K. F., De Smedt, I., and van der A, R. J.: Assessing the distribution and growth rates of NO<sub>x</sub> emission sources by inverting a 10-year record of NO<sub>2</sub> satellite columns, *Geophys. Res. Lett.*, 35, 1–5, doi:10.1029/2008GL033521, 2008.
- Stavrakou, T., Müller, J.-F., Boersma, K. F., van der A, R. J., Kurokawa, J., Ohara, T., and Zhang, Q.: Key chemical NO<sub>x</sub> sink uncertainties and how they influence top-down emissions of

987 nitrogen oxides, *Atmos. Chem. Phys.*, 13, 9057–9082, <https://doi.org/10.5194/acp-13-9057-2013>,  
988 2013.

989

990 Super, I., Dellaert, S. N. C., Visschedijk, A. J. H., and Denier van der Gon, H. A. C.:  
991 Uncertainty analysis of a European high-resolution emission inventory of CO<sub>2</sub> and CO to support  
992 inverse modelling and network design, *Atmos. Chem. Phys.*, 20, 1795–1816,  
993 <https://doi.org/10.5194/acp-20-1795-2020>, 2020.

994

995 Szopa, S., Foret, G., Menut, L., and Cozic, A.: Impact of large scale circulation on  
996 European summer surface ozone: consequences for modeling, *Atmospheric Environment*, 43, 1189–  
997 1195, doi:10.1016/j.atmosenv.2008.10.039, 2008.

998

999 Talagrand, O. : Assimilation of observations : an introduction, *J. Met. Soc., Japan*, 75,  
1000 191-209, 1997.

1001

1002 Tang, X., ZhuJ., WangZ.F., WangM., GbaguidiA., LiJ., ShaoM., TangG. Q., and JiD.S.:  
1003 Inversion of CO emissions over Beijing and its surrounding areas with ensemble Kalman filter,  
1004 *Atmospheric Environment*, 81, 676-686, 2013.

1005

1006 Valin, L. C., Russell, A. R., and Cohen, R. C.: Variations of OH radical in an urban  
1007 plume inferred from NO<sub>2</sub> column measurements, *Geophys. Res. Lett.*, 40, 1856–1860,  
1008 doi:10.1002/grl.50267, 2013.

1009

1010 van der A, R. J., Eskes, H. J., Boersma, K. F., van Noije, T. P. C., van Roozendael, M., De  
1011 Smedt, I., Peters, D. H. M. U., and Meijer, E. W.: Trends, seasonal variability and dominant NO<sub>x</sub>  
1012 source derived from a ten year record of NO<sub>2</sub> measured from space, *J. Geophys. Res.*, 113, 1–12,  
1013 doi:10.1029/2007JD009021, 2008.

1014

1015 Vestreng, V., Breivik, K., Adams, M., Wagner, A., Goodwin, J., Rozovskaya, O.,  
1016 and Oacyna, J.: Inventory Review 2005 - Emission Data reported to CLRTAP and under the NEC  
1017 Directive - Initial review for HMs and POPs .EMEP Status report, Norwegian Meteorological  
1018 Institute, Oslo, 2005.

1019

1020 Vinken, G. C. M., Boersma, K. F., Maasakkers, J. D., Adon, M., and Martin, R. V.:  
1021 Worldwide biogenic soil NO<sub>x</sub> emissions inferred from OMI NO<sub>2</sub> observations, *Atmos. Chem.*  
1022 *Phys.*, 14, 10363–10381, <https://doi.org/10.5194/acp-14-10363-2014>, 2014.

1023

1024 Yin, Y., Chevallier, F., Ciais, P., Broquet, G., A. Fortems-Cheiney, Pison, I. and Saunois,  
1025 M: Decadal trends in global CO emissions as seen by MOPITT, *Atmos. Chem. Phys.*, 15, 13433–  
1026 13451, 2015.

1027

1028 Yumimoto, K. and Uno, I.: Adjoint inverse modeling of CO emissions over Eastern Asia  
1029 using four-dimensional variational data assimilation, *Atmospheric Environment*, 40, 35, 6836-6845,  
1030 DOI: 10.1016/j.atmosenv.2006.05.042, 2006.

1031

1032 Wang, Y., G. Broquet, P. Ciais, F. Chevallier, F. Vogel, N. Kadyrov, L. Wu, Y. Yin, R.  
1033 Wang and S. Tao: Estimation of observation errors for large-scale atmospheric inversion of  
1034 CO<sub>2</sub> emissions from fossil fuel combustion, *Tellus B: Chemical and Physical Meteorology*, 69:1,  
1035 DOI: [10.1080/16000889.2017.1325723](https://doi.org/10.1080/16000889.2017.1325723), 2017.

1036

1037 Wang, Y., Broquet, G., Ciais, P., Chevallier, F., Vogel, F., Wu, L., Yin, Y., Wang, R., and  
1038 Tao, S.: Potential of European <sup>14</sup>CO<sub>2</sub> observation network to estimate the fossil fuel CO<sub>2</sub> emissions



1039 via atmospheric inversions, *Atmos. Chem. Phys.*, 18, 4229–4250, [https://doi.org/10.5194/acp-18-](https://doi.org/10.5194/acp-18-4229-2018)  
1040 4229-2018, 2018.

1041

1042 WHO World Health Organization: Ambient Air Pollution: a global assessment of  
1043 exposure and burden of disease, 2016.

1044

1045 Zheng, T., French, N. H. F., and Baxter, M.: Development of the WRF-CO<sub>2</sub> 4D-Var  
1046 assimilation system v1.0, *Geosci. Model Dev.*, 11, 1725–1752, [https://doi.org/10.5194/gmd-11-](https://doi.org/10.5194/gmd-11-1725-2018)  
1047 1725-2018, 2018.

1048

1049 Zheng, B., Chevallier, F., Yin, Y., Ciais, P., Fortems-Cheiney, A., Deeter, M. N., Parker,  
1050 R. J., Wang, Y., Worden, H. M., and Zhao, Y.: Global atmospheric carbon monoxide budget 2000–  
1051 2017 inferred from multi-species atmospheric inversions, *Earth Syst. Sci. Data*, 11, 1411–1436,  
1052 <https://doi.org/10.5194/essd-11-1411-2019>, 2019.

1053